



**HAL**  
open science

# Modeling High-Pressure Hydrogen Uptake by Nanoporous Metal-Organic Frameworks: Implications for Hydrogen Storage and Delivery

Pamela Ramirez-Vidal, Rafael L S Canevesi, Alain Celzard, Vanessa Fierro

► **To cite this version:**

Pamela Ramirez-Vidal, Rafael L S Canevesi, Alain Celzard, Vanessa Fierro. Modeling High-Pressure Hydrogen Uptake by Nanoporous Metal-Organic Frameworks: Implications for Hydrogen Storage and Delivery. ACS Applied Nano Materials, 2022, 5 (1), pp.759-773. 10.1021/acsnm.1c03493 . hal-03842569

**HAL Id: hal-03842569**

**<https://hal.univ-lorraine.fr/hal-03842569v1>**

Submitted on 7 Nov 2022

**HAL** is a multi-disciplinary open access archive for the deposit and dissemination of scientific research documents, whether they are published or not. The documents may come from teaching and research institutions in France or abroad, or from public or private research centers.

L'archive ouverte pluridisciplinaire **HAL**, est destinée au dépôt et à la diffusion de documents scientifiques de niveau recherche, publiés ou non, émanant des établissements d'enseignement et de recherche français ou étrangers, des laboratoires publics ou privés.

# **Modeling High-Pressure Hydrogen Uptake by Nanoporous Metal-Organic Frameworks: Implications for Hydrogen Storage and Delivery**

Pamela Ramirez-Vidal, Rafael L. S. Canevesi, Alain Celzard, Vanessa

Fierro\*

Université de Lorraine, CNRS, IJL, 88000 Epinal, France

\* Corresponding author. Tel: + 33 329 29 61 77.

Fax: + 33 329 29 61 38.

E-mail address: [Vanessa.Fierro@univ-lorraine.fr](mailto:Vanessa.Fierro@univ-lorraine.fr) (V. Fierro)

## Abstract

Due to their very high porosity and superior textural properties, metal organic frameworks (MOFs) are promising nanoporous materials for hydrogen storage by cryo-compression. Herein, we investigated hydrogen adsorption on four commercial MOFs, namely MIL53-Al, MOF-5, HKUST-1, and MOF-177, over a temperature range of 77 to 273 K and pressures up to 14 MPa. The Modified Dubinin-Astakhov (MDA) equation was used to fit the experimental adsorption data, and six parameters ( $m$ ,  $n_{max}$ ,  $\alpha$ ,  $\beta$ ,  $P_0$  and  $V_a$ ) were obtained. We concluded that the parameters  $n_{max}$  and  $V_a$  are related to the micropore volume while  $\alpha$ ,  $\beta$ ,  $m$  and  $P_0$  are related to the average micropore size. Compared to hydrogen compression in an empty tank, the introduction of MOF-5 enhanced the volumetric hydrogen storage at 77 K and 10 MPa from 31 to 42 kg m<sup>-3</sup>. The release H<sub>2</sub> capacities of MOFs from a loading pressure of 10 MPa to a discharge pressure of 0.5 MPa were determined for either isothermal discharge at 77 K or after temperature increase to 160 K. For MOF-5, the amount of usable hydrogen increased up to 10.6 wt.% (40.8 mg cm<sup>-3</sup>) by pressure drop (from 10 to 0.5 MPa) and temperature increase (from 77 to 160 K).

**Keywords:** hydrogen storage; metal-organic-framework; adsorption modelling; high-pressure adsorption; release capacity; adsorption entropy.

## List of symbols and abbreviation

$\Delta h_{ads}$	Isosteric enthalpy of adsorption
$\Delta n_{H_2}^{77K \rightarrow 160K}$	H <sub>2</sub> release capacity from 10 MPa and 77 K to 0.5 MPa and 160 K
$\Delta n_{H_2}^{77K \rightarrow 77K}$	H <sub>2</sub> release capacity from 10 to 0.5 MPa at 77 K
2D-NLDFT-HS	2D non-local density functional theory for heterogeneous surface
$A_{BET}$	BET area
$A_{BET Ar}$	BET area calculated from the Ar adsorption data
$A_{BET N_2}$	BET area calculated from the N <sub>2</sub> adsorption data
$\bar{d}_T$	Average pore diameter
$\bar{d}_\mu$	Average micropore diameter
DA	Dubinin-Astakhov
$K_H$	Henry's law constant
$m$	Exponent related to the heterogeneity of the material
MDA	Modified Dubinin-Astakhov
$n_{abs}$	Absolute hydrogen uptake
$n_{exc}$	Excess hydrogen uptake
$n_{max}$	Adsorbed hydrogen uptake, equivalent to the saturation of the entire available pore volume according the MDA Model
$n_{tot}$	Total hydrogen uptake
$n_{tot}^{back P}$	Total hydrogen uptake at the back pressure (usually fuel cell pressure, 0.5 MPa)
$n_{tot}^{max P}$	Total hydrogen uptake at the maximum tank pressure (10 MPa in this study)
$P$	Equilibrium pressure
$P/P^\circ$	Relative pressure
$P_0$	Pseudo-saturation pressure
$P^\circ$	Saturation pressure (0.1 MPa)
PSD	Pore size distribution
$Q_{st}^{MDA}$	Isosteric heat of adsorption from the MDA equation
$R$	Universal gas constant
$S_{<0.7 nm, NLDFT}$	Specific surface area in the ultramicropore range
$S_{0.7-2nm, NLDFT}$	Specific surface area in the supermicropore range
$S_{NLDFT}$	surface area determined by applying the NLDFT model
$T$	Equilibrium temperature

$V_{<0.7nm,NLDFT}$	Ultramicropore volume determined by applying the NLDFT model
$V_{0.7-2nm,NLDFT}$	Supermicropore volume determined by applying the NLDFT model
$V_a$	Volume of the adsorbed phase
$V_{DA, Ar}$	Micropore volume determined by applying the DA model to the Ar adsorption isotherm
$V_{meso}$	Mesopore volume determined by applying the NLDFT model
$V_{micro}$	Micropore volume determined by applying the NLDFT model
$V_T$	Total pore volume reported in the literature and determined from Ar or N <sub>2</sub> adsorption at $P/P^\circ = 0.97-0.99$ .
$V_{T, Ar}$	Total pore volumes determined from Ar adsorption at $P/P^\circ = 0.97$
$V_{T, N_2}$	Total pore volumes determined from N <sub>2</sub> adsorption at $P/P^\circ = 0.97$
$V_{T, NLDFT}$	NLDFT total pore volumes from the
$V_v$	Void volume
$\alpha$	Enthalpy factor in the MDA equation
$\beta$	Entropy factor in the MDA equation
$\theta$	Surface coverage
$\rho_a$	Adsorbed phase density
$\rho_{cry}$	Single-crystal density
$\rho_g$	Gas density
$\rho_{pack}$	Packing density
$\rho_{sk}$	Skeletal density
$\rho_{TAP}$	Tapped density

## 1. Introduction

Hydrogen is a promising green energy carrier, as it has the highest gravimetric energy density of all non-nuclear fuels (*i.e.*,  $120 \text{ MJ kg}^{-1}$  compared to  $47 \text{ MJ kg}^{-1}$  for petroleum) <sup>1</sup>. It can be used to power fuel cell vehicles (FCVs) and produces no  $\text{CO}_2$  emissions because its only combustion product is  $\text{H}_2\text{O}$ . However, one of the main technical obstacles limiting the large-scale use of FCVs is the huge volume of  $\text{H}_2$  needed to achieve a driving autonomy of 500 km when the gas is at standard conditions (*e.g.*  $61 \text{ m}^3$  at 298 K and 0.1 MPa) <sup>1,2</sup>. Therefore, the current objective is to design hydrogen storage systems that are rapidly rechargeable, compact, lightweight and cost-effective <sup>2,3</sup>. To increase the volumetric energy density of hydrogen, different approaches have been studied: (i) compression in gas cylinders <sup>1</sup>; (ii) liquefaction in cryogenic tanks <sup>4</sup>, (iii) cryo-compression <sup>2</sup> and; (iv) absorption by - or adsorption on - solids (*i.e.*, metal hydrides <sup>5</sup>, nanostructured carbons<sup>6</sup>, hyper-crosslinked polymers <sup>7</sup> and metallic organic frameworks <sup>8,9</sup>).

Pressure in cryogenic hydrogen storage can be significantly reduced by introducing a microporous material (pore diameter  $< 2 \text{ nm}$ ) to enhance hydrogen adsorption <sup>6,10</sup>. This approach has several advantages over  $\text{H}_2$  storage by compression or liquefaction. For instance, it requires lower strength materials compared to those needed at 70 MPa and 298 K <sup>2</sup>. As a result, cryogenic pressure vessels are lighter, more compact and more cost-effective than gas compression storage systems. The cost of cryogenic tanks is currently estimated at  $\$390 \text{ kg}^{-1}$  <sup>4</sup>. In addition, cryo-compression overcomes the gas losses associated with boiling in  $\text{H}_2$  liquefaction systems <sup>2,11</sup>, which are very energy-intensive, accounting for at least one-third of the energy contained in hydrogen <sup>11</sup>. Indeed, unlike cryogenic tanks of liquefied  $\text{H}_2$ , cryogenic pressure tanks significantly extend the period of dormancy, as the vehicle is powered by an additional 48 watt-

days<sup>2</sup>. Finally, the higher temperatures and lower pressures employed in cryogenic pressure vessels offer potential safety advantages over compressed gas vessels and cryogenic tanks. Recently, the Hydrogen Storage Engineering Centre of Excellence (HSECoE) has proposed the design of cryogenic adsorption pressure tanks to charge hydrogen to 77 K and 10 MPa and discharge it at 160 K and 0.5 MPa<sup>12</sup>. Indeed, the use of these operating conditions could be advantageous for several reasons. For example, 10 MPa is the highest refueling pressure for Type I all-metal cryogenic pressure vessels<sup>8</sup>, which are the least expensive pressure vessels available. In addition, 0.5 MPa is chosen as the discharging pressure because it is approximately the pressure at which there is no longer a gradient driving hydrogen flow to the engine<sup>8</sup>.

Due to their very high porosity and unique textural properties, nanoporous metal organic frameworks (MOFs) have been investigated over the past two decades as suitable materials for hydrogen storage<sup>8,13-15</sup>. In addition to their developed textural properties, the perfectly ordered open channels present in MOFs allow efficient access of hydrogen molecules to the inner space<sup>9,13</sup>, thus reducing diffusion problems at cryogenic temperatures. Modelling hydrogen isotherms of MOFs is essential for the efficient design of hydrogen storage systems based on adsorption-desorption<sup>2,8,16</sup>. Indeed, the analytical representation of the experimental data over the whole operating pressure and temperature is necessary to calculate the complete mass and energy conservation equations<sup>16</sup>. The Sips<sup>10</sup>, Toth<sup>17</sup> and the Modified Dubinin-Astakhov (MDA)<sup>6,10,16,18-21</sup> equations have been used to fit the hydrogen uptake as a function of temperature and pressure in MOFs. The MDA equation was found to fit well the H<sub>2</sub> adsorption isotherms on MOF-5<sup>16,22</sup> and MOF-177<sup>19</sup> over a wide range of temperatures (50-300 K) and pressures (0.1-70 MPa)<sup>16,19</sup>. In the latter studies, the relationship between MDA parameters and textural

characteristics was not established, however, but we have seen that this relationship exists as revealed in a recent study dealing with hydrogen storage in activated carbons.

Herein, H<sub>2</sub> adsorption on four commercial MOFs (*i.e.*, MIL-53 Al, HKUST-1, MOF-5 and MOF-177) was performed between 77 and 213 K and up to 14 MPa. The six parameters of the MDA equation (*i.e.*,  $m$ ,  $n_{max}$ ,  $\alpha$ ,  $\beta$ ,  $P_0$  and  $V_a$ ) were obtained by fitting adsorption data from eleven isotherms with eleven adsorption points for each MOF. As volumetric hydrogen adsorption capacity is important to ensure non-bulky final systems, gravimetric and volumetric uptakes of H<sub>2</sub> were determined together with the deliverable capacity.

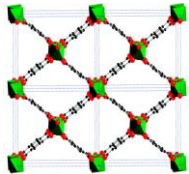
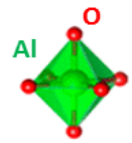
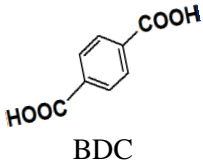
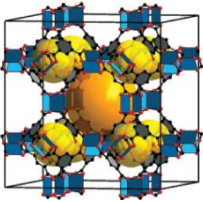
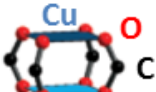
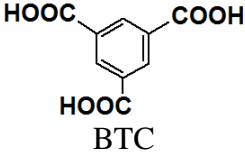
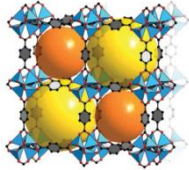
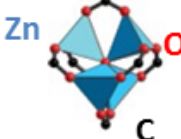
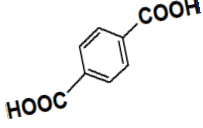
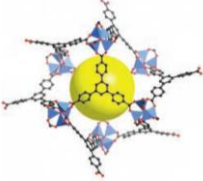
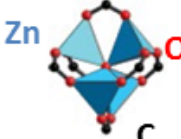
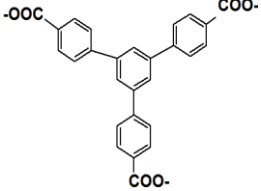
## 2. Experimental

### 2.1 MOFs

Four metal organic frameworks (MOFs) were studied, namely: (i) MIL-53 Al (C<sub>8</sub>H<sub>5</sub>AlO<sub>5</sub>) from Sigma-Aldrich; (ii) HKUST-1 (C<sub>18</sub>H<sub>6</sub>Cu<sub>3</sub>O<sub>12</sub>) from Sigma-Aldrich; (iii) MOF-5 (C<sub>24</sub>H<sub>12</sub>O<sub>13</sub>Zn<sub>4</sub>) from Nanoshel®; and (iv) MOF-177 (C<sub>54</sub>H<sub>30</sub>O<sub>13</sub>Zn<sub>4</sub>) from Sigma-Aldrich. **Table 1** shows the formula, structure, secondary building units (SBUs), linker and single-crystal density,  $\rho_{cry}$ , of the selected MOFs.



**Table 1.** Characteristics of the MOFs selected for this study.

MOF	Formula	Structure <sup>a</sup>	SBU <sup>b</sup>	Linker <sup>c</sup>	$\rho_{\text{cry}}^{\text{d}}$ ( $\text{cm}^3 \text{g}^{-1}$ )
MIL-53Al	$\text{C}_8\text{H}_5\text{AlO}_5$		 $\text{AlO}_4(\text{OH})_2$	 BDC	0.978 <sup>23</sup>
HKUST-1	$\text{C}_{18}\text{H}_6\text{Cu}_3\text{O}_{12}$		 $\text{Cu}_2(-\text{COO})_4$	 BTC	0.879 <sup>15</sup>
MOF-5	$\text{C}_{24}\text{H}_{12}\text{O}_{13}\text{Zn}_4$		 $\text{Zn}_4\text{O}(\text{CO}_2)_6$	 BDC	0.590 <sup>24,25</sup>
MOF-177	$\text{C}_{54}\text{H}_{30}\text{O}_{13}\text{Zn}_4$		 $\text{Zn}_4\text{O}(\text{CO}_2)_6$	 BTB	0.430 <sup>25-27</sup>

<sup>a</sup> The structure of MIL-53AL was reprinted with permission from <sup>28</sup>. Copyright © 2021 American Chemical Society. The structure of MOF-177 was reproduced from <sup>29</sup> with permission from the Wiley online Library. The structures of MOF-5 and HKUST-1 were reproduced from <sup>30</sup> with permission from the Wiley online Library.

<sup>b</sup> The secondary building units of the MIL-53Al was adapted with permission from <sup>31</sup>. Copyright © 2021 American Chemical Society; whereas, the ones of the HKUST-1, MOF-5 and MOF-177 were adapted from <sup>30</sup> with permission from the Wiley online Library.

<sup>c</sup> The linker abbreviation corresponds to: 1,4-benzenedicarboxylic acid (BDC); 1,3,5-benzenetricarboxylic acid (BTC); and 4,4',4''-benzene-,3,5-triyltribenzoate (BTB)

<sup>d</sup> Single-crystal density and corresponding reference(s).

## 2.2 Textural characterization

Textural characterization of MOFs was performed by physisorption of N<sub>2</sub>, CO<sub>2</sub>, H<sub>2</sub> and Ar at 77, 273, 77 and 87 K, respectively, in a Micromeritics® 3-flex manometric device. Prior to the gas adsorption experiments, the MOFs were outgassed under vacuum ( $< 10^{-4}$  Pa) at 383 K for more than 48h. The BET area ( $A_{BET}$ ) was determined from the N<sub>2</sub> and Ar isotherms using Micromeritics® Microactive software and applying the Rouquerol criteria<sup>32</sup>. To assess the pore size distribution (PSD) of MOFs, the 2D non-local density functional theory (2D-NLDFT-HS) for cylindrical pores (Me-type zeolite) was applied to the Ar isotherms using SAIEUS® software (Micromeritics) in agreement with previous studies<sup>33,34</sup>. From their PSDs, we found the specific surface areas ( $S_{NLDFT}$ ), ultramicropore surface areas ( $S_{<0.7nm,NLDFT}$ ), supermicropore surface areas ( $S_{0.7-2nm,NLDFT}$ ), ultramicropore volumes ( $V_{<0.7nm, NLDFT}$ ), supermicropore volumes ( $V_{0.7-2nm,NLDFT}$ ), mesopore volumes ( $V_{mes}$ ), total pore volumes ( $V_{T, NLDFT}$ ), average pore diameters ( $\bar{d}_T$ ) and average micropore diameters ( $\bar{d}_\mu$ ). Additionally, the total pore volumes  $V_{T, N_2}$  and  $V_{T, Ar}$  were determined from N<sub>2</sub> and Ar adsorption isotherms, respectively, at relative pressures  $p/p^\circ = 0.97$ . For comparison, the micropore volumes were also determined using the Dubinin-Astakhov (DA) equation<sup>35</sup> applied to the Ar adsorption data, and they were referred to as  $V_{DA, Ar}$ .

## 2.3 Hydrogen adsorption at high pressure

Hydrogen isotherms were performed up to 14 MPa at 77, 93, 113, 133, 153, 173, 193, 213, 233, 253 and 273 K in a Micromeritics® HPVAII automatic adsorption equipment coupled to a single-stage closed cycle cryogenic refrigerator; more details have been reported elsewhere<sup>6,10</sup>. Briefly, approximately 1.2 g of the selected MOF was loaded into a 10 cm<sup>3</sup> cell and outgassed under vacuum ( $6 \times 10^{-4}$  Pa) at 383 K for 48h. The isotherms were performed with precise

temperature control to  $\pm 0.005$  K. Adsorption pressures steps were measured at 0.1, 0.5, 0.8, 1, 2, 3, 5, 7.5, 10, 12.5 and 14 MPa, whereas desorption data were obtained at 11.5, 8, 4.5, 1.5 and 0.5 MPa.

## **2.4 Skeletal and tapped density determination**

Prior to measurement of skeletal and tapped density, the samples were degassed at 383 K under primary vacuum overnight. The skeletal density of the samples was measured by He pycnometry in a Micromeritics® AccuPyc II 1340 instrument at room temperature. Tapped densities of the samples were obtained in a Quantachrome® Autotap apparatus. Briefly, approximately 4 mL of MOF powder was poured into a 10 mL-measuring cylinder and mechanically tapped 1500 times in at least two cycles. If a variation of more than 5% was observed between the volumes obtained in the first two cycles, a third determination was performed. Then, the tapped density of the MOF was calculated as the mass of the sample divided by the final volume.

## **3. Modeling**

### **3.1 Experimental determination of the adsorbed phase density**

When hydrogen is adsorbed onto a porous material, a density profile is formed in the pores. Near the pore walls, the adsorbed hydrogen has a higher density that is generally considered to be close to that of liquid hydrogen<sup>36,37</sup>. However, some authors have considered that the density of supercritical hydrogen adsorbed in nanoporous solids may be higher than that of the liquid phase and closer to that of solid hydrogen<sup>38-41</sup>. The density of molecules inside the pores decreases with distance from the surface, to a minimum that is equal to the density of the free gas at system

pressure<sup>40</sup>. Therefore,  $n_{abs}$  [mol kg<sup>-1</sup>] is defined as the absolute amount of gas confined in a volume,  $V_a$ , which is the volume of adsorbed gas<sup>42</sup>. Furthermore,  $n_{exc}$  [mol kg<sup>-1</sup>] is defined as the difference between  $n_{abs}$  at a specific pressure and temperature, and the amount that would be present under the same conditions in  $V_a$ , and in the absence of adsorption.  $n_{abs}$  and  $n_{exc}$  are related by Eq. (1), where  $\rho_g$  [mol m<sup>-3</sup>] is the hydrogen density in the gas phase at the same conditions of pressure and temperature:

$$n_{abs} = n_{exc} + \rho_g V_a \quad (1)$$

Assuming that  $V_a$  varies according to  $V_a = n_{abs}/\rho_a$ , where  $\rho_a$  [mol m<sup>-3</sup>] is the hydrogen density in the adsorbed phase, Eq. (1) can be expressed as follows:

$$n_{exc} = n_{abs} \left( 1 - \frac{\rho_g}{\rho_a} \right) \quad (2)$$

Generally speaking,  $n_{exc}$  and  $n_{abs}$  are almost identical up to 0.1 MPa because  $\rho_g \ll \rho_a$ . When the gas is compressed, the term  $\rho_g/\rho_a$  becomes non-negligible and consequently,  $n_{exc}$  exhibits a maximum, which occurs when  $\rho_a$  monotonically approaches a constant value while  $\rho_g$  continues to increase as the pressure<sup>37</sup>. After the maximum,  $n_{exc}$  decreases significantly and eventually reaches the so-called saturation regime at  $\rho_g/\rho_a \gg 1$  where, considering that the adsorbed phase has a non-compressible fluid behavior and that there is no phase change in the saturation regime,<sup>19,20,43</sup> Eq. (2) can be approximated by Eq. (3):

$$\frac{\partial n_{exc}}{\partial \rho_g} \cong -V_a \quad (3)$$

Therefore,  $V_a$  can be calculated as the absolute value of the slope when plotting  $n_{exc}$  as a function of  $\rho_g$ , as in Eq. (4), for pressures higher than those needed for reaching the maximum  $n_{exc}$ :

$$n_{exc} = n_{abs} - \rho_g V_a \quad (4)$$

At the intercept with the  $x$ -axis ( $n_{exc} = 0$ ), the gas and the adsorbed phase have the same density ( $\rho_g = \rho_a$ ), and hence it is possible to estimate the density of the adsorbed phase as a function of temperature<sup>20,37,43</sup>.

### 3.2 Application of the Modified Dubinin-Astakhov (MDA) equation

$n_{exc}$  can be suitably represented by the modified Dubinin-Astakhov (MDA) equation<sup>16,19,20</sup>, which reads as follows:

$$n_{exc} = n_{max} \exp \left[ - \left( \frac{RT}{\alpha + T\beta} \right)^m \ln^m \left( \frac{P_0}{P} \right) \right] - \rho_g V_a \quad (5)$$

where  $n_{max}$  [mol kg<sup>-1</sup>] is the limiting hydrogen uptake corresponding to the maximum filling of the entire volume of adsorption space,  $R$  [8.314 J mol<sup>-1</sup> K<sup>-1</sup>] is the molar gas constant,  $\alpha$  [J mol<sup>-1</sup>] is the “enthalpy” factor,  $\beta$  [mol J<sup>-1</sup> K<sup>-1</sup>] is the “entropy” factor<sup>19</sup>,  $T$  [K] is the temperature of the isotherm,  $P$  [MPa] is the equilibrium pressure,  $P_0$  [MPa] is the pseudo-saturation pressure according to Dubinin’s definition<sup>35</sup>, and  $m$  is an exponent related to the heterogeneity of the material.  $\rho_g$  was obtained from REFPROP-7 software and the  $n_{exc}$  data set, experimentally determined for each MOF at the eleven temperatures selected in this study, was fitted simultaneously to obtain the six MDA parameters ( $m$ ,  $n_{max}$ ,  $\alpha$ ,  $\beta$ ,  $P_0$  and  $V_a$ ) using the Levenberg-Marquardt algorithm<sup>44</sup>.

### 3.3 Determination of the isosteric heats of adsorption from the MDA equation

According to the Clausius-Clapeyron equation<sup>21</sup>, the isosteric heat of adsorption,  $Q_{st}^{MDA}$  [J mol<sup>-1</sup>], or isosteric enthalpy of adsorption,  $-\Delta h_{ads}$  [J mol<sup>-1</sup>], can be calculated as follows:

$$\Delta h_{ads} = -RT^2 \left[ \frac{\partial \ln P}{\partial T} \right]_{n_a, V} \quad (6)$$

From the MDA equation Eq. (5),  $\ln(P)$  can be expressed as follows:

$$\ln(P) = - \left( \frac{\alpha + T\beta}{RT} \times \left( - \ln \left( \frac{n_{abs}}{n_{max}} \right) \right)^{\frac{1}{m}} \right) + \ln(P_0) \quad (7)$$

and from Eq. (7),  $\left[ \frac{\partial \ln P}{\partial T} \right]_{n_a, V}$  can be determined as follows:

$$\left[ \frac{\partial \ln P}{\partial T} \right]_{n_a, V} = (\alpha R^{-1} T^{-2}) \left( - \ln \left( \frac{n_{abs}}{n_{max}} \right) \right)^{\frac{1}{m}} \quad (8)$$

Therefore,  $Q_{st}^{MDA}$  can be determined by merging Eq. (6) and Eq. (8) and replacing  $n_{abs}/n_{max}$  by  $\theta$ , which is the surface coverage at the surface of the MOFs, leading to Eq. (9). This equation is in good agreement with that reported by Richard et al.<sup>21</sup> for activated carbons when  $m$  is equal to 2.

$$-\Delta h_{ads} = Q_{st}^{MDA} = \alpha \left( - \ln(\theta) \right)^{\frac{1}{m}} \quad (9)$$

### 3.4 Total usable capacity

The total hydrogen uptake is defined as all the hydrogen present in the material, regardless of whether it is adsorbed or compressed. The total hydrogen uptake,  $n_{tot}$ , can be calculated from Eq. (10) where  $n_{exc}$  [mol kg<sup>-1</sup>] is the excess uptake,  $\rho_{pack}$  [kg m<sup>-3</sup>] is the packing density of the (granular or powdered) porous adsorbent material,  $\rho_{sk}$  [kg m<sup>-3</sup>] is the skeleton density of the latter, and  $\rho_g$  [mol m<sup>-3</sup>] is the gas phase density.  $n_{exc}$  uptakes were calculated using the parameters found from the MDA equation, and the  $\rho_g$  data were obtained from the REFPROP-7 software. In addition, either the tapped density ( $\rho_{TAP}$ ) or the single-crystal density ( $\rho_{cry}$ ) were used as values for packing densities ( $\rho_{pack}$ ) to calculate the total hydrogen uptakes. Although the use of the

tapped density would lead to more realistic estimates<sup>13</sup>, most studies in the open literature used the single-crystal density of the materials<sup>8,9,15,45,46</sup>, which can be determined by XRD analysis. Yet, it is clear that if one makes the crude approximation that  $\rho_{pack} = \rho_{cry}$ , this means that one neglects the void volume of the granular adsorbent packing, which significantly reduces the estimated contribution of the H<sub>2</sub> compression  $\left( \left( \frac{1}{\rho_{pack}} - \frac{1}{\rho_{skel}} \right) \rho_{gas} \right)$  in Eq. (10). We therefore considered it more realistic to assume the bed of granular material as a regular, close-packing of spherical grains when the single-crystal density is employed in the calculations. The compactness of such a packing is 74%<sup>47</sup>, and therefore, the packing density is assumed to be 74% of the single-crystal density, *i.e.*,  $\rho_{pack} = 0.74 \rho_{cry}$ .

$$n_{tot} = n_{exc} + \left( \frac{1}{\rho_{pack}} - \frac{1}{\rho_{skel}} \right) \rho_{gas} \quad (10)$$

Furthermore, in practical applications, the cryogenic compression adsorption system should be able to adsorb and also release as much hydrogen as possible under the operating conditions<sup>8,15,45</sup>. Therefore, the usable amount of stored H<sub>2</sub><sup>45,48</sup>, or release capacity<sup>8,9,15</sup>,  $\Delta n_{H_2}$  [mol kg<sup>-1</sup>], can be calculated as follows:

$$\Delta n_{H_2} = n_{tot}^{max P} - n_{tot}^{back P} \quad (11)$$

where  $n_{tot}^{max P}$  [mol kg<sup>-1</sup>] is the total hydrogen uptake at the charging, maximum, tank pressure, and  $n_{tot}^{back P}$  [mol kg<sup>-1</sup>] is the total hydrogen uptake at the discharge pressure, *i.e.*, the minimum back pressure for a fuel cell. The deliverable capacity,  $\Delta n_{H_2}$ , was calculated considering a discharge pressure (back pressure) of 0.5 MPa, which is usually considered as the lower limit for having hydrogen flow from a tank to an engine<sup>12,15</sup>. The charging pressure was

estimated to be 10 MPa, as this is the highest refueling pressure for all-metal Type I tanks<sup>8</sup>. Two scenarios were considered: an isothermal charge-discharge process<sup>15</sup> ( $\Delta n_{H_2}^{isothermic}$ ) at 77 K, and a temperature change from a loading at 77 K to a discharge at 160 K ( $\Delta n_{H_2}^{77-160 K}$ ).



## 4. Results and discussion

### 4.1 Textural characterization

**Figure 1**, **Figure S1** and **Table S1** show the results of textural characterization of the studied MOFs. According to the IUPAC classification<sup>49</sup>, MOF-5, HKUST-1 exhibit Type Ia isotherms for Ar and N<sub>2</sub> adsorption at 77 and 87 K, respectively (**Figure 1a** and **Figure S1**). This type is characteristic of purely microporous materials with narrow pore diameters, less than 0.7 nm. The Ar and N<sub>2</sub> isotherms of MOF-177 and MIL-53Al show a combination of Types Ia and IV, which is typical of micro-mesoporous materials. These observations concerning the porosity are in good agreement with the PSDs obtained by application of the 2D-NLDFT-HS model. PSD results are displayed in **Table S1** and **Figure 1b**. For instance, the fraction of microporosity, calculated as  $V_{micro\ NLDFT} / V_{T, NLDFT}$ , of MOF-5 and HKUST-1 was 100%, while MOF-177 and MIL-53 Al presented 7.2 and 34.7 % of mesoporosity, respectively. The total volume of pores,  $V_{T\ NLDFT}$ , decreased in the order MOF-177 > MOF-5 > HKUST-1 > MIL-53 Al (1.66, 1.06, 0.78 and 0.43 cm<sup>3</sup> g<sup>-1</sup>, respectively).

**Figure S2a** and **Table S1** show the values of  $V_{T\ N_2}$  and  $V_{T\ Ar}$  obtained by the N<sub>2</sub> and Ar isotherms at  $p/p^\circ = 0.97$ , and those of  $V_{T\ NLDFT}$  for the four MOFs. Minor differences are observed between  $V_{T\ Ar}$  and  $V_{T\ NLDFT}$  (< 1 % for MIL-53 Al, MOF-5 and MOF-177; and 7% for HKUST-1). In general, larger total pore volumes were obtained when N<sub>2</sub> adsorption was used (**Figure S2a**), which can be attributed to the specific interactions of N<sub>2</sub> with the metal ions due to its significant quadrupole moment<sup>34</sup>. Having no quadrupole moment, Ar is a more reliable probe to characterize the texture of MOFs<sup>34,49</sup>. In addition, Ar is more suitable for characterizing microporous materials since at this temperature, Ar fills narrow pores at significantly higher relative pressures than N<sub>2</sub> at 77 K<sup>49</sup>.

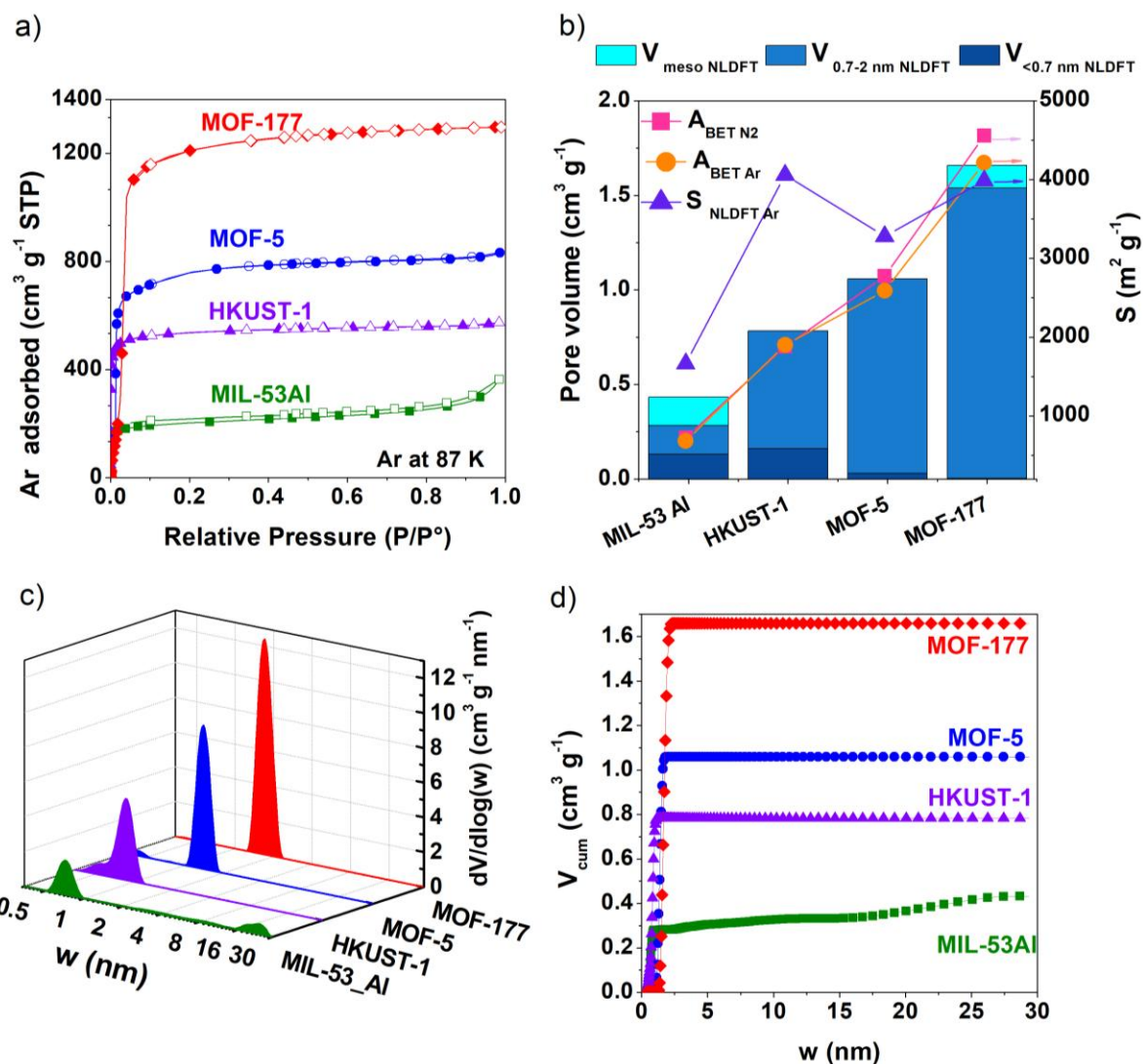


**Figure 1.** Textural characteristics of the MOFs studied here: (a) Ar adsorption–desorption isotherms at 87 K; (b)  $A_{BET}$  obtained from  $N_2$  and Ar adsorption,  $S_{NLDFT}$ , and pore volumes in the ultramicropore (< 0.7 nm), supermicropore (0.7–2 nm) and mesopore (2–50 nm) ranges; (c) pore size distributions; and (d) cumulative pore volumes from the 2D-NLDFT fits to the Ar isotherms.

The values of  $A_{BET}$  from the  $N_2$  and Ar adsorption data were in the ranges of 727–4557 and 681–4215  $m^2 g^{-1}$ , respectively (**Table S1**). As for the total pore volume, in general, the values of  $A_{BET N_2}$  were higher than those of the corresponding  $A_{BET Ar}$  due to the specific interactions between nitrogen and the metal ions. Larger differences were observed when comparing  $A_{BET Ar}$

and  $S_{NLDFT}$  due to the limitations of the BET theory that overestimates or underestimates the surface area<sup>49</sup>. Overestimation occurs when there is a developed texture with large micropores ( $1 < d < 2$  nm) and mesopores, since  $N_2$  uptake proceeds by pore filling and not by monolayer adsorption<sup>50,51</sup>. The underestimation is related to the existence of ultramicropores in the material ( $< 0.7$  nm) where only a monolayer of nitrogen is taken into account<sup>34</sup>.

The values of  $S_{NLDFT}$ , in the range of 1666-4061  $m^2 g^{-1}$ , were always higher than those obtained for  $A_{BET Ar}$  (**Figure 1b** and **Table S1**). The difference varied from 5 to 26% for MOF-177 and MOF-5, respectively, but was considerably higher for HKUST-1 and MIL-53Al, where  $S_{NLDFT}$  was at least two times higher than  $A_{BET Ar}$ . We have to take into account that, having different metals in their composition (Zn for MOF-177 and MOF-5, and Cu and Al for HKUST-1 and MIL-53Al, respectively), the interactions between the hydrogen molecules and the metallic ions are not equivalent for all materials. In addition, we took a kernel developed for metal-exchanged zeolites because a kernel for MOFs has not yet been developed. We are aware of the limitations of this approach; nevertheless, we show below that the application of this 2D-NLDFT-HS model allows us to obtain relationships between parameters related to hydrogen storage and textural characterization. **Figure S2b** shows the micropore volumes obtained by the DA and NLDFT models using Ar adsorption. Minor differences, up to 10%, were observed between  $V_{DA, Ar}$  and  $V_{micro NLDFT}$  values.

All the MOFs present a quite narrow PSD with a main peak in the range of 1.25-2.3, 1.05-1.81, 0.37-1.15 and 0.51-0.95 nm for MOF-177, MOF-5, HKUST-1 and MIL-53Al, respectively (**Figure 1c**). Furthermore, the sample MIL-53Al exhibits a small peak at 16.8-30.6 nm, which corresponds to the presence of mesopores. In good agreement with **Figure 1c**, most of the pore volume of the samples is microporous (**Figure 1d**).  $\bar{d}_\mu$  varies from 0.73 to 1.65 nm and increases

in the order MIL-53Al < HKUST-1 < MOF-5 < MOF-177, while  $\bar{d}_T$  varies from 0.81 to 6.23 nm and increases in the order HKUST-1 < MOF-5 < MOF-177 < MIL-53Al (**Table S1**). MIL-53Al thus has the narrowest  $\bar{d}_\mu$  and the widest  $\bar{d}_T$ , due to the considerable relative amount of wide mesopores (see again **Figure 1d**).

#### 4.2 CO<sub>2</sub> and H<sub>2</sub> adsorption at atmospheric pressure

The CO<sub>2</sub> and H<sub>2</sub> isotherms at 273 and 77 K obtained up to 0.1 MPa are shown in **Figure S2a-b**. To date, most studies performed on gas storage have focused on gravimetric uptake of materials<sup>7,10,52-56</sup>, although knowledge of volumetric uptakes is essential for the assessment of storage systems<sup>8,9,15</sup>. Therefore, CO<sub>2</sub> and H<sub>2</sub> volumetric uptakes at 0.1 MPa were calculated using the tapped density of the MOFs and were reported in **Table S2** together with the correspondent gravimetric uptakes. Gravimetric and volumetric gas uptakes linearly increased with  $V_{<0.7\text{ NLDFT}}$  (**Figure 2c** and **Table S2**), which is related to the fact that gas adsorption under atmospheric pressure mainly depends on the narrowest pores, *i.e.*, those where adsorption forces are enhanced due to overlapping adsorption potentials of the two pore walls<sup>49,57,58</sup>.

At low pressures, in the Henry's law region, the gas concentration is low enough to consider that all adsorbed molecules are isolated from their nearest neighbors and that their intermolecular interactions can be neglected<sup>59</sup>. In this region, the excess uptaked,  $n_{exc}$  [wt.%], increases linearly with pressure, and the proportionality constant is known as Henry's law constant  $K_H$  [wt.% kPa<sup>-1</sup>]. **Figure 2d-e** shows the CO<sub>2</sub> and H<sub>2</sub> isotherms up to 10 kPa where the uptake increases linearly with pressure ( $R^2 > 0.98$ ). Up to 10 kPa (**Figure 2d-e**), the gas uptake increases in the order MOF-177 < MOF-5 < MIL-53Al < HKUST-1, in relation to their values of  $V_{<0.7\text{ NLDFT}}$ , whereas at 0.1 MPa MOF-5 and MOF-177 have similar uptakes. The Henry's constants of H<sub>2</sub> ( $K_{H\text{ H}_2}$ ) and

CO<sub>2</sub> ( $K_{H\text{CO}_2}$ ) at 77 and 273 K (**Table S3**) were estimated as the slopes of the solid lines plotted in **Figure 2d-e**. The pressure region taken in the linear fit and the  $R^2$  of the experimental data are reported in **Table S3**. Since Van der Waals interactions are stronger in MOFs with narrower pores<sup>49,57,58</sup>, Henry's constants  $K_{H\text{CO}_2}$  and  $K_{H\text{H}_2}$  linearly increase with  $V_{<0.7\text{NLDFT}}$ . In good agreement,  $K_{H\text{CO}_2}$  and  $K_{H\text{H}_2}$  increase when reducing the average micropore size,  $\bar{d}_\mu$  (**Figure S3a-b**). The good agreement of the results with the expected behavior of the adsorption phenomena corroborates that the PSDs obtained are representative of the MOFs texture.

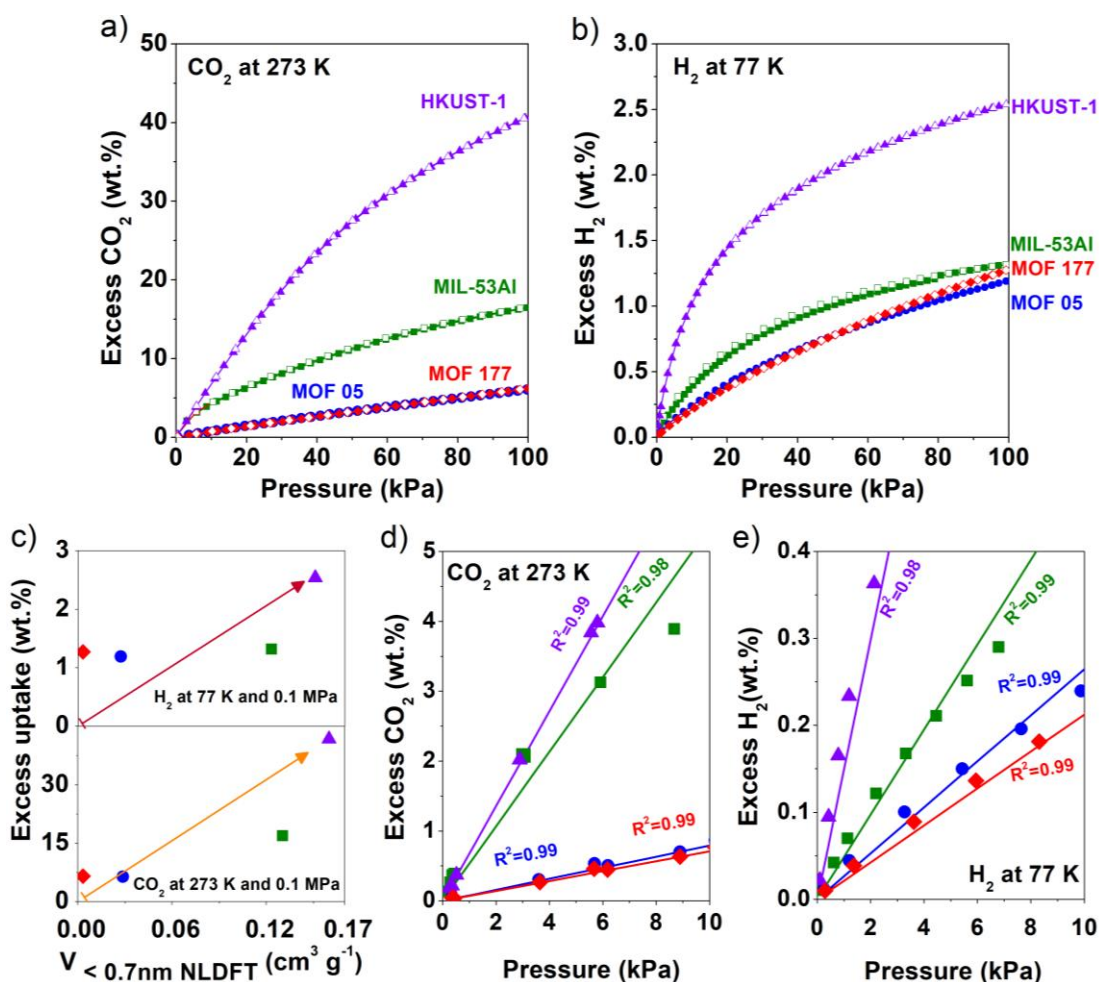


**Figure 2.** a) CO<sub>2</sub> isotherms at 273 K up to 100 kPa; b) H<sub>2</sub> isotherms at 77 K up to 100 kPa; c) H<sub>2</sub> and CO<sub>2</sub> excess uptakes at 0.1 MPa plotted as a function of  $V_{<0.7}$ ; d) CO<sub>2</sub> isotherms at 273 K up to 10 kPa; and e) H<sub>2</sub> isotherms at 77 K up to 10 kPa. In (c)-(e), the symbols have the same meaning as in (a)-(b).

### 4.3 Hydrogen adsorption at high pressure

The adsorption of H<sub>2</sub> on the four MOFs was fully reversible over the ranges of temperature (77-273 K) and pressure (0.1-15 MPa) studied. **Figure 3** shows the H<sub>2</sub> adsorption-desorption isotherms at the lowest temperature, 77 K (**Figure 3a**) and at the highest one, 273 K (**Figure 3b**), for the four MOFs. In **Figure 3a-b**, no hysteresis loop is observed as the desorption points (empty symbols) overlap with the adsorption points (filled symbols) over the entire pressure range.

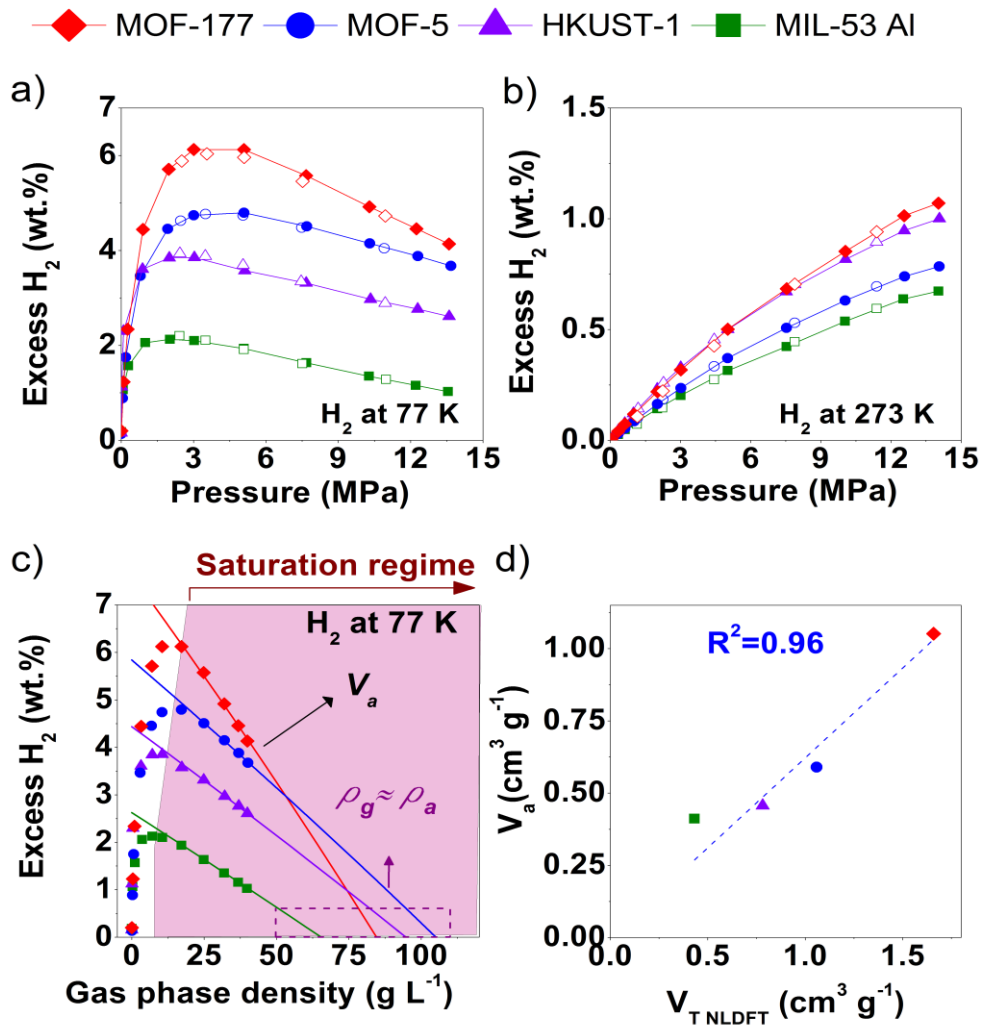


**Figure 3.** Excess hydrogen isotherms: a) at 77 K; and b) at 273 K, for the four MOFs. Filled and empty symbols correspond to adsorption and desorption data, respectively. c) Excess H<sub>2</sub>

uptake expressed as a function of gas phase density at 77 K; and d) evolution of  $V_a$  with  $V_{TNLDFT}$ .

At 77 K and 2-3 MPa, the H<sub>2</sub> excess isotherm shows a maximum value of 6.1, 4.7, 3.8, 2.1 wt.% for MOF-177 (at 3 MPa), MOF-5 (3 MPa), HKUST-1 (2 MPa) and MIL-53Al (2 MPa), respectively (**Figure 3a** and **Table S4**). The values of H<sub>2</sub> excess uptakes at 273 K and 14 MPa were 1.1, 0.8, 1.0, 0.7 wt.% for MOF-177, MOF-5, HKUST-1 and MIL-53Al, respectively (**Figure 3b** and **Table S5**). The maximum H<sub>2</sub> excess uptake observed in the 2-3 MPa range (**Figure 3a**) corresponds to the point where the gas phase density,  $\rho_g$ , increases while the adsorbed phase density,  $\rho_a$ , approaches monotonically a constant value<sup>37</sup>. Indeed, when the gas is compressed,  $\rho_g$  increases significantly and  $\rho_g/\rho_a$ , see Eq. (2), becomes non-negligible. After the maximum, the excess H<sub>2</sub> decreases significantly with increasing  $\rho_g$  and finally reaches the saturation regime<sup>19,20,43</sup> where the excess uptake decreases linearly with  $\rho_g$  as shown in **Figure 3c**.

The results of the linear regression of the curves in the saturation regime are reported in **Table S6**. The  $R^2$  of the linear regression were greater than 0.996, which means that  $\rho_a$  does not vary significantly with pressure in the saturation regime and that the adsorbed phase behaves as an incompressible fluid<sup>20</sup>. Given the critical point of H<sub>2</sub> ( $T_c = 33$  K and  $P_c = 0.13$  MPa), we can assume that there is no phase change beyond the measured region<sup>19,20,43</sup> and extrapolate the curves to their intercept with the  $x$ -axis where  $n_{exc} = 0$  (**Figure 3c**). At that point and according to Eq. (2), the gas and the adsorbed phase have the same densities ( $\rho_g = \rho_a$ )<sup>20,37,43</sup>, so it is possible to estimate the density of the adsorbed phase (**Table S6**).  $\rho_a$  at 77 K and high pressure was found to be around 81, 105, 99 and 65 kg m<sup>-3</sup> for MOF-177, MOF-5, HKUST-1 and MIL-53Al, respectively (**Table S6** and **Figure 3c**). For MIL-53 Al,  $\rho_a$  approaches the density of

hydrogen at the boiling point (about  $70 \text{ kg m}^{-3}$ ) while  $\rho_a$  in HKUST-1 approaches the density of solid hydrogen ( $86 \text{ kg m}^{-3}$ ).  $\rho_a$  for MOF-177 and MOF-5 are significantly higher than the density of solid hydrogen, in good agreement with some authors<sup>38-41</sup> who reported the solid-like behavior of the adsorbed hydrogen phase. These high values are not completely surprising if we consider that the limiting adsorption corresponds to a point where the density of the adsorbed phase is at its maximum, and where the latter becomes incompressible. Indeed, Romanos et al.<sup>40</sup> reported that the density of the hydrogen adsorbed in nanopores can be higher than that of the solid phase, up to  $100 \text{ kg m}^{-3}$ . The  $V_a$  values obtained from the linear regression of Eq. (4) are presented in **Table S6**. According to the results discussed in Section 4.1,  $\rho_a$  is higher in MOFs with narrower pores due to the strong Van der Waals interactions between the pore walls (**Figure S4**).

Furthermore,  $V_a$  was found to be directly proportional to  $V_{T \text{ NLDFT}}$  (**Figure 3d**) and to  $A_{BET \text{ Ar}}$  (**Figure S5**) with  $R^2$  of 0.96 and 0.90, respectively, when the data were fitted through the origin (0,0). This is in agreement with the results we found in a previous study on commercial activated carbons<sup>6</sup>, where  $V_a$  obtained from the fit of the MDA equation to the data was proportional to  $V_{T \text{ NLDFT}}$  and  $A_{BET}$ . The good correlation of  $V_a$  with  $A_{BET}$  also shows that the BET method is sometimes more indicative of the volume than the surface area itself. **Figure S5** and **Table S7** show the linear relationship between  $A_{BET}$  and  $V_T$  for the four MOFs studied and for other MOFs reported in recent studies<sup>8,9,15,27,45,60,61</sup>.

**Figure 4a-b** shows the hydrogen excess uptakes at high pressure and 77 K (2-3 MPa) and 273 K (14 MPa) adsorbed as a function of  $A_{BET \text{ Ar}}$  (**Figure 4a**) and  $S_{\text{NLDFT}}$  (**Figure 4b**). Fits made by forcing the linear regressions through (0,0) are shown in red and green dashed lines for adsorption performed at 77 and 273 K, respectively. At 2-3 MPa and 77 K (**Figure 4a**), a high  $R^2$



was obtained when  $n_{exc}$  was plotted as a function of  $A_{BET Ar}$  ( $R^2 = 0.89$ ) but a much lower value ( $R^2 = 0.41$ ) was obtained for the uptakes at 273 K and 14 MPa. This is related to the fact that using the BET model<sup>62</sup>, pore filling and not just monolayer adsorption is considered for the determination of  $A_{BET}$ <sup>49,63</sup> and pore filling is enhanced at 77 K. At 77 K, a similar  $R^2$  was found when  $n_{exc}$  was plotted as a function of  $S_{NLDFT}$  (**Figure 4b**), in good agreement with published results<sup>8,13</sup>. At 273K, the amount of hydrogen adsorbed is much lower than at 77 K, the entire pore volume is not occupied and thus the amount of hydrogen is more related to surface than volume. Since the NLDFT method gives a better estimate of the surface area, the determination factor increases from 0.41 to 0.93 using  $A_{BET}$  and  $S_{NLDFT}$ , respectively, to establish the correlation.

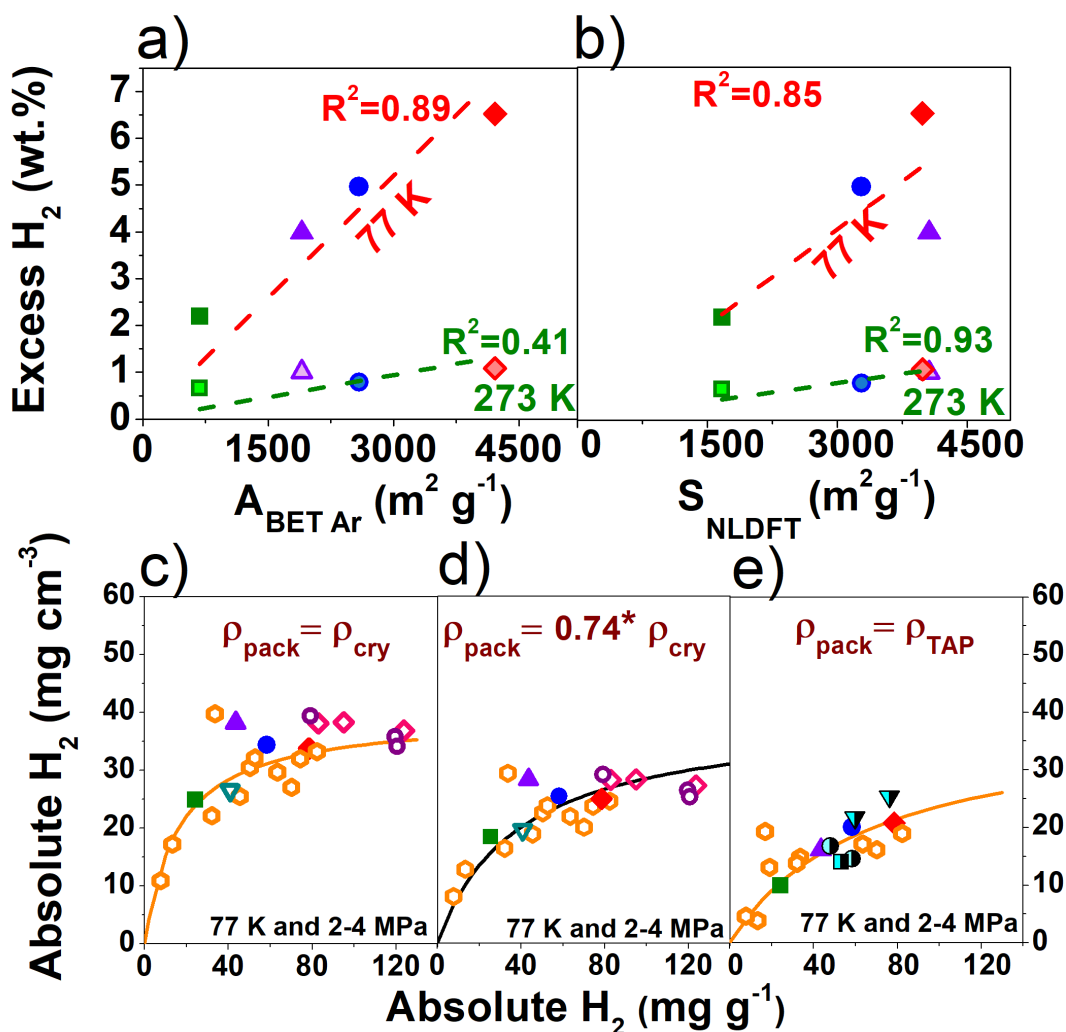


**Figure 4.** Hydrogen excess at 77 K and 2-3 MPa (■ MIL-53AL, ● MOF-5, ▲ HKUST-1, ◆ MOF-177 and ---) and 273 K and 14 MPa (■ MIL-53AL, ● MOF-5, ▲ HKUST-1, ◆ MOF-177 and ---) as a function of (a)  $A_{BET Ar}$  and (b)  $S_{NLDFT}$ . The dashed lines (---) correspond to the linear regression fit through the origin at (0,0). Volumetric vs. gravimetric absolute hydrogen uptakes of porous materials using as the packing density: (c) the single-crystal density; (d) 74 % of the single-crystal density; and (e) the tapped density, from recent studies on activated carbons (●<sup>10</sup>, ■<sup>64</sup>, ▼<sup>65</sup>), MOFs (○<sup>13</sup>, ▼<sup>27</sup>, ○<sup>8</sup>, ◆<sup>9</sup>) and this study (■ MIL-53AL, ● MOF-5, ▲ HKUST-1, ◆ MOF-177). The orange line (-) in (c) and (e) correspond to the model proposed by Balderas-Xicohténcatl et al.<sup>13</sup>. The black line (-) in (d) is only a guide for the eye. The absolute uptake from the excess reported data was calculated using REPROF software to calculate the H<sub>2</sub> gas density and considering the adsorbed phase volume as the total pore volume.

Actually, excess hydrogen adsorption at 77 K was found to increase by 0.8 wt. % per 500 m<sup>2</sup> g<sup>-1</sup> of  $A_{BET Ar}$ , which could be proposed as an alternative to the Chahine rule<sup>13,51,66</sup> for MOFs. It

may be useful to recall here that Chahine's rule, initially found for ACs, states that  $n_{exc}$  increases by 1 wt.% per  $500 \text{ m}^2 \text{ g}^{-1}$  of  $A_{BET N_2}$ .  $n_{exc}$  was also found to be directly proportional to  $V_{T NLDFT}$  and  $V_{micro}$  (**Figure S6a-b**). The linear relationship of  $n_{exc}$  with  $V_{T NLDFT}$  indicates that supermicropores and even narrow mesopores are highly relevant for enhancing hydrogen uptake at 77 K and high pressure<sup>6,67</sup>. At 77 K and pressures above 2 MPa, the excess  $\text{H}_2$  uptake decreased in the order  $\text{MOF-177} > \text{MOF-5} > \text{HKUST-1} > \text{MIL-53Al}$  (**Figure 3a**), which is different from that observed at 77 K and up to 0.1 MPa (**Figure 2**). This highlights the fact that at high pressure, not the same pores are relevant to enhance the adsorption process.

**Table S7** shows textural properties, tapped and single-crystal densities from recent studies on MOFs. Recent studies have found a linear relationship between specific surface area and pore volume (**Table S7**) and an inverse relationship between volumetric surface area (which is equal to  $A_{BET} \times \rho_{pack}$ ) and void volume in MOFs<sup>13,14</sup>. These results imply that the volumetric and gravimetric absolute uptakes are related<sup>13</sup>. **Figure 4c-d** show the absolute volumetric and gravimetric hydrogen uptakes at 77 K and 2-4 MPa on MOFs from the open literature (data shown in **Table S8**). Absolute uptakes from excess reported data were calculated using the approximation  $V_{pore} \approx V_a$  and employing the gas density calculated from the REPROF software. To quantify the volumetric uptake, either the single-crystal density (**Figure 4c and d**) or the tapped density (**Figure 4e**) were employed. Indeed, the use of tapped density could lead to more realistic estimations of the packed column volume<sup>13</sup>, however, for most of the studies in the open literature, the tapped density is not available and the packing density is considered equal to the single-crystal density<sup>8,9,15,45,46</sup>. **Figure 4c** and **Table S8** display the absolute uptakes on a volumetric basis, which have been reported in recent studies in the literature under the assumption  $\rho_{pack} = \rho_{cry}$ . This assumption neglects the loss in  $\text{H}_2$  storage capacity due to packing

<sup>13,15,45,60</sup> because the material is considered to behave as a monolithic block and not as a stack of granular material. Consequently, higher volumetric uptakes are obtained compared to those calculated using the tapped density (**Figure 4e**). **Figure 4d** shows the absolute uptakes on gravimetric and volumetric basis when the materials are assumed to behave as a regular close-packing of spherical grains<sup>47</sup> ( $\rho_{pack} = 0.74 \rho_{cry}$ ). Although this assumption remains an idealization of real granular materials packing, it provides values in better agreement with those obtained when the tapped density is employed (**Figure 4e**).

Regarding the relationship between the volumetric and gravimetric absolute uptakes, Balderas-Xicohténcatl et al.<sup>13</sup> proposed Eq. (12), whose parameters have the following meaning.  $n_{abs}^{vol}$  [ $\text{mg cm}^{-3}$ ] is the volumetric absolute uptake and  $n_{abs}^{grv}$  [ $\text{mg g}^{-1}$ ] is the gravimetric absolute uptake.  $a$  [ $4.8 \times 10^{-4} \text{ cm}^3 \text{ m}^{-2}$ ] is a constant related to the ratio of total pore volume to specific surface area in the MOFs,  $k$  [ $1.9 \times 10^{-2} \text{ mg m}^{-2}$ ] is a constant related to the hydrogen surface density (at high pressures and 77 K), and  $v_0$  [ $\text{cm}^3 \text{ g}^{-1}$ ] is a constant parameter of the model that has been related to the specific skeleton volume in MOFs. The value of the latter parameter is 1.7 or  $0.4 \text{ cm}^3 \text{ g}^{-1}$  depending on whether tapped density or single-crystal density is used in the model. Indeed, the skeleton volume of the material and the void volume between its grains account for the value of  $v_0$  and, therefore,  $v_0$  is larger when using the tapped density because the void volume between grains is not considered in the single-crystal density.

$$n_{abs}^{vol} = \frac{n_{abs}^{grv}}{\frac{a}{k} n_{abs}^{grv} + v_0} \quad (12)$$

**Figure 4c-d** shows the absolute volumetric uptake as a function of absolute gravimetric uptake for our data and literature data<sup>8-10,13,27,64,65</sup>. The absolute H<sub>2</sub> adsorption on a volumetric basis tends to plateau at the highest values of absolute gravimetric H<sub>2</sub> uptake, in particular for

materials with high BET areas <sup>13</sup>. Our data in **Figure 4c-d** are properly predicted by the equation proposed by Balderas-Xicohténcatl et al <sup>13</sup>, represented by the orange solid line.

#### 4.4 Application of the MDA equation

**Figure 5** shows the experimental hydrogen isotherms (full and empty symbols correspond to adsorption and desorption data, respectively) of the four MOFs studied here, and their fits with the MDA equation. The six parameters of the MDA equation (*i.e.*,  $m$ ,  $n_{max}$ ,  $\alpha$ ,  $\beta$ ,  $P_0$  and  $V_a$ ) found by non-linear regression of hydrogen adsorption data are listed in **Table S9**. The  $R^2$  coefficient was on average between 0.96 and 0.98 for the four MOFs (**Table S9**), which shows that the MDA equation fitted the experimental data adequately, as we already found for H<sub>2</sub> adsorption on CACs <sup>6</sup> In the latter study, we found that the MDA parameters were related to the textural properties of the CACs. In this section, we will examine the relationship between the MDA parameters and the textural parameters of MOFs and CACs.

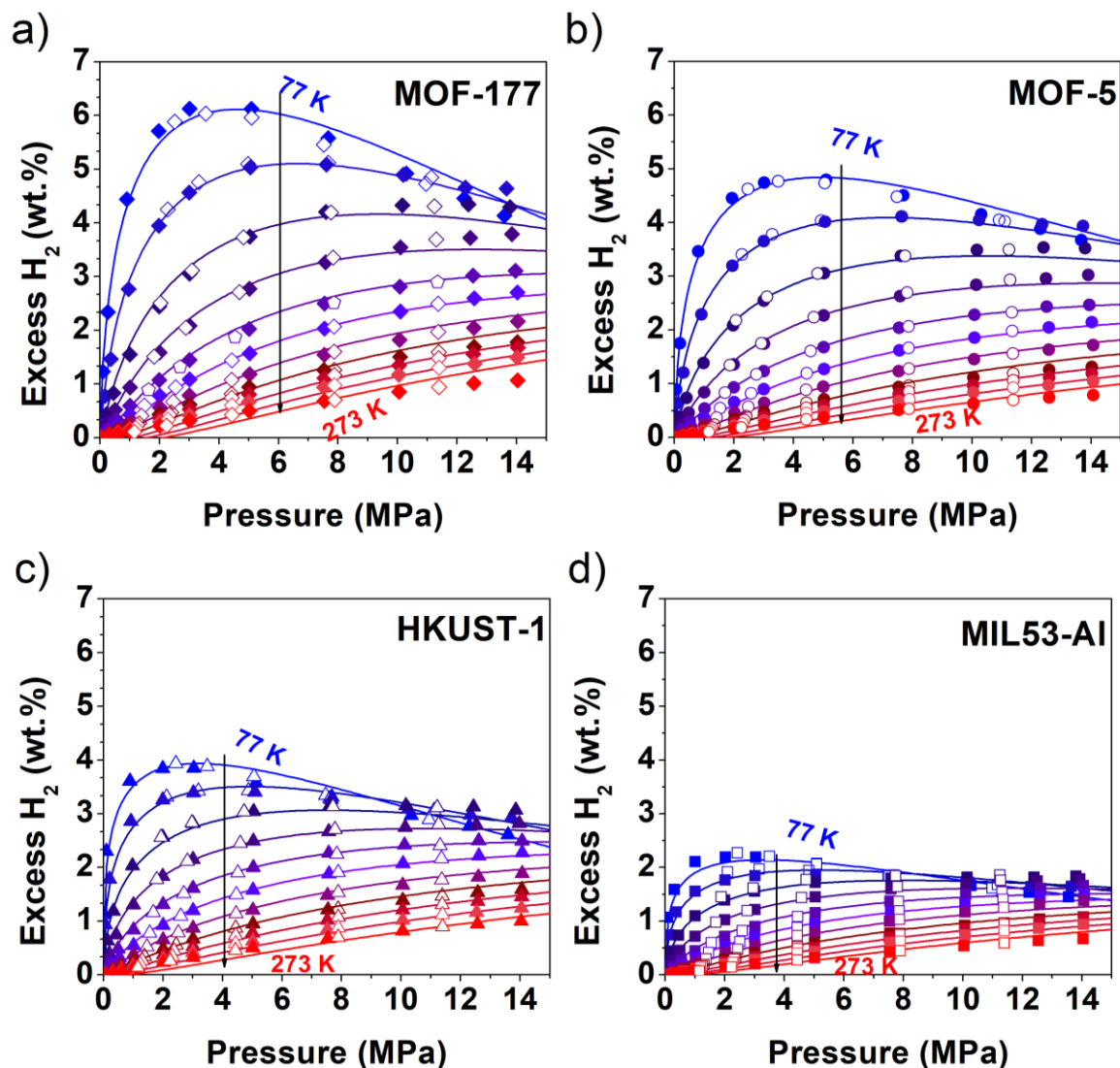


**Figure 5.** Hydrogen isotherms on: (a) MOF 177; (b) MOF-5; (c) HKUST-1; and (d) MIL-53 Al, and their fits with the MDA equation at 77, 93, 113, 133, 153, 173, 193, 213, 233, 253 and 273 K. Full and empty symbols indicate adsorption and desorption data, respectively.

**Table S10** shows the values of  $R^2$  when the MDA parameters were linearly fitted to the different textural parameters. **Figure 6** shows the MDA parameters of MOFs (this study) and CACs (from <sup>6</sup>) plotted as a function of  $A_{BET}$  ( $n_{max}$  and  $V_a$ ), and  $\bar{d}_\mu$  ( $\alpha$ ,  $\beta$ ,  $P_0$  and  $m$ ).  $n_{max}$  ranged from 115.7 to 20.3 mol kg<sup>-1</sup> and increased linearly with  $A_{BET}$ ,  $V_{T, NLDFT}$  and  $S_{NLDFT}$  (**Figure 6a** and **Table S10**). This is in line with the linear increase of  $n_{exc}$  with  $V_{T, NLDFT}$  and  $A_{BET}$  discussed in

Section 4.2 (**Figure 4a** and **Figure S6a**). Recently, a study published by Zhang. et al.<sup>51</sup> demonstrated the correlation between pore volume and hydrogen capacity on MOFs using two empirical equations, in good agreement with the linear increase of  $n_{max}$  with  $V_{T, NLDFT}$  found here.  $V_a$  ranged from 0.56 to 2.42 cm<sup>3</sup> g<sup>-1</sup> and was also proportional to  $A_{BET}$ ,  $V_{T, NLDFT}$  and  $S_{NLDFT}$  (**Figure 6b** and **Table S10**). The fact that higher R<sup>2</sup> were found when  $A_{BET}$  rather than  $S_{NLDFT}$  was used indicates that hydrogen storage at high pressure is not exclusively a surface phenomenon but also a pore-filling phenomenon. In fact, due to the assumptions of the BET model<sup>62</sup>,  $A_{BET}$  is an apparent area that takes into account not only surface coverage but also pore filling<sup>49,63</sup> and thus,  $n_{max}$  and  $V_a$  increase proportionally to it. The values of  $V_a^{DA}$  obtained from the MDA model were larger than those of  $V_a^{plot}$  obtained by the linear regression of the  $n_{exc}$  curves at 77 K (**Figure S7**) (see Section 4.2), which could be attributed to the empirical nature of the MDA model. In fact,  $V_a$  values reported in the literature are as high as 1.94<sup>22</sup> and 2.84<sup>16</sup> cm<sup>3</sup> g<sup>-1</sup> for MOF-5, and 3.30<sup>19</sup> cm<sup>3</sup> g<sup>-1</sup> for MOF-177.

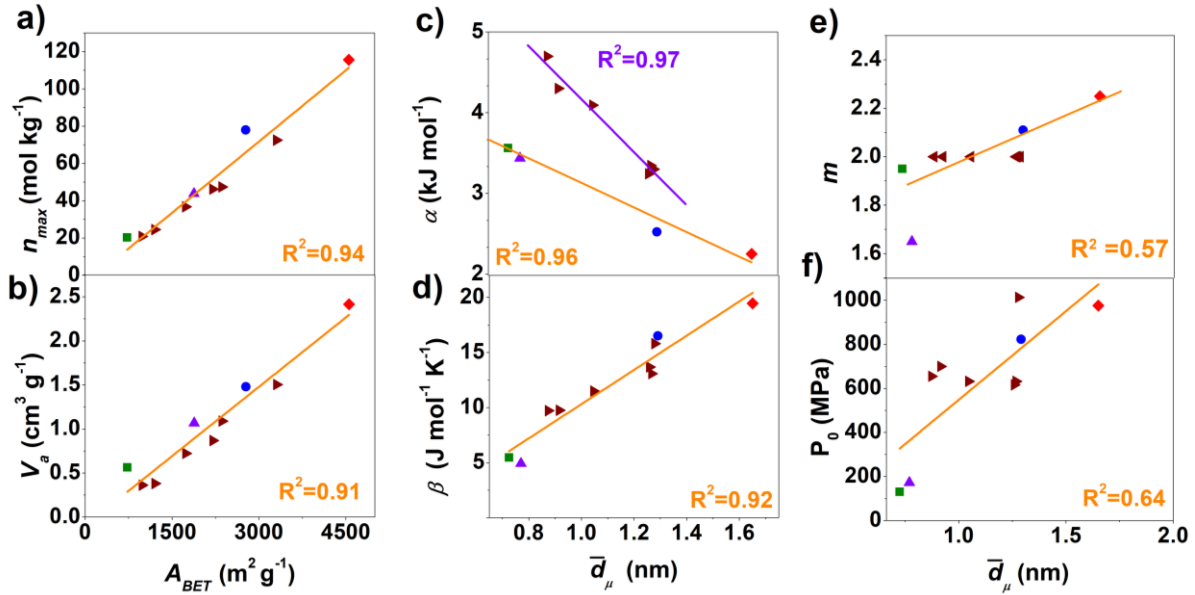


**Figure 6.** DA parameters of MOFs (■ MIL-53AL, ● MOF-5, ▲ HKUST-1, ◆ MOF-177) and CACs <sup>6</sup> ►, plotted against two textural parameters: (a)  $V_a$  and (b)  $n_{max}$  as a function of  $A_{BET}$ ; and (b)  $\alpha$ , (c)  $\beta$ , (e)  $m$  and (f)  $P_0$  as a function of  $\bar{d}_\mu$ .

**Figure 6c-d** shows the  $\alpha$  and  $\beta$  parameters of MOFs and CACs <sup>6</sup> plotted as a function of the average micropore size ( $\bar{d}_\mu$ ). Both series of data decrease progressively as  $\bar{d}_\mu$  increases, with an  $R^2$  of 0.97 and 0.96 for CACs and MOFs, respectively (**Figure 6c**). The parameter  $\alpha$  is usually named the enthalpy factor <sup>10,21</sup>, as it is related to the isosteric heat of adsorption ( $Q_{st}$ ) by Eq. (9). **Figure 7** shows the isosteric heat of adsorption,  $Q_{st}^{MDA}$ , as a function of the surface coverage,  $\theta = n_{abs}/n_{max}$  (**Figure 7a**) and the average micropore size,  $\bar{d}_\mu$  (**Figure 7b**). For each of the MOFs studied,  $Q_{st}^{MDA}$  increases with  $\theta$  (**Figure 7a**). Indeed, at low  $\theta$ , the first sites to be occupied are those with the strongest interactions (and higher  $Q_{st}$ ) with  $H_2$  molecules, mainly the ultramicropores (**Figure 7b**). Subsequently, as the sites are filled and  $\theta$  increases,  $H_2$  is adsorbed in wider pores where the interactions are less strong and consequently  $Q_{st}^{MDA}$  decreases <sup>6,51</sup>. Nevertheless, Eq. (9) is not suitable for calculating  $Q_{st}^{MDA}$  when  $\theta$  approaches 0 and 1 because it



is mathematically limited to the range  $0 < \theta < 1$ . Indeed,  $Q_{st}^{MDA}$  increases indefinitely or becomes zero when  $\theta$  approaches 0 and 1 respectively.

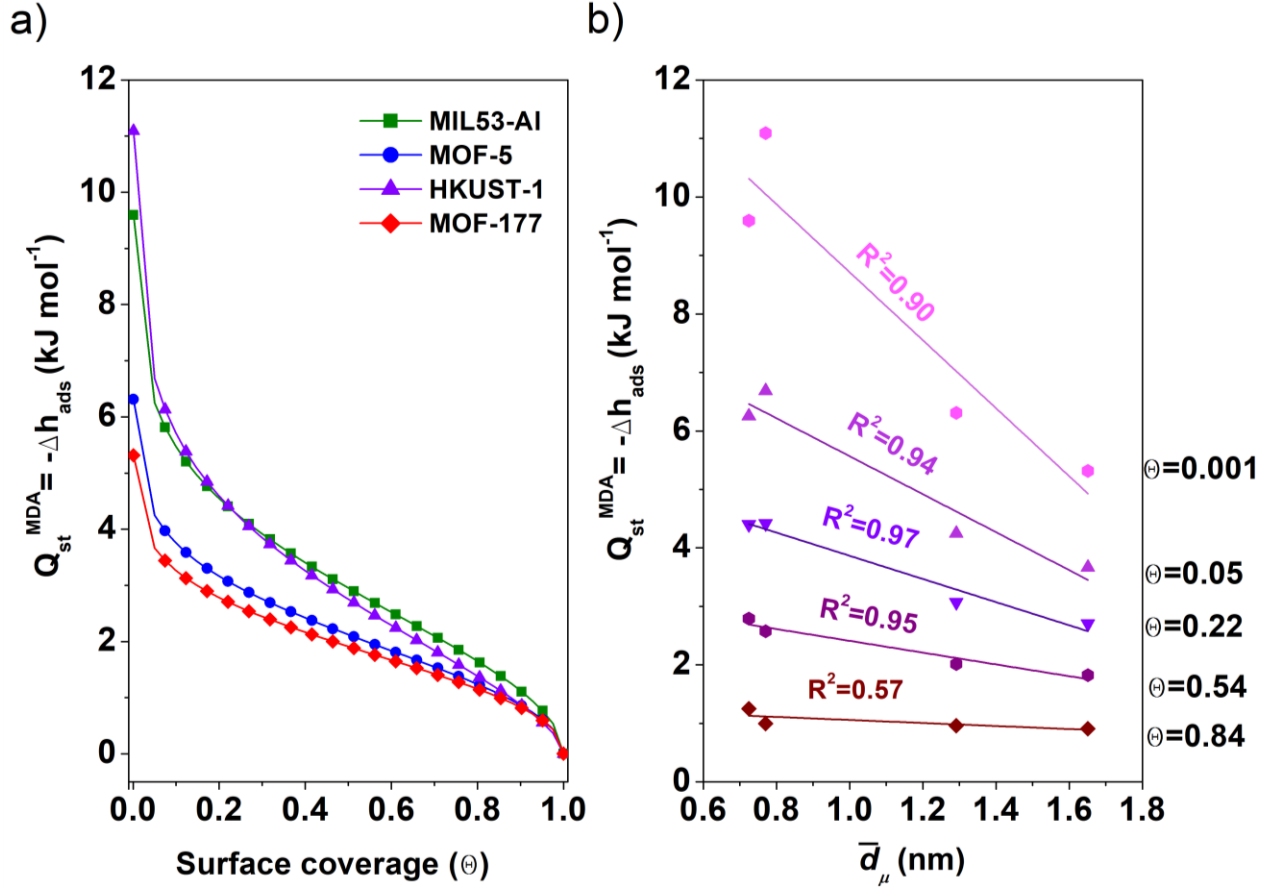


**Figure 7.** Evolution of  $Q_{st}^{MDA}$  as a function of: (a) surface coverage; and (b) average micropore size for several surface coverages.

The isosteric heat of adsorption,  $Q_{st}$ , is related to the Van der Waals interactions between the solid surface and the gas, which depend on the pore diameter but also on the surface chemistry<sup>34,49,57</sup>. Therefore, it is logical that the evolutions of  $\alpha$  with  $\bar{d}_\mu$  for MOFs and CACs are not fitted with the same linear regression (**Figure 6c**) because their chemical nature is very different. The average  $Q_{st}$  values for MOFs are in good agreement with those of MOF-177<sup>64</sup> (around 4 kJ mol<sup>-1</sup> at  $0.02 < \theta < 0.8$ ) and DUT-23 (Co)<sup>27</sup> (around 4 kJ mol<sup>-1</sup> at  $0.02 < \theta < 0.8$ ). The average  $Q_{st}$

values for the CAC called AX-21 <sup>10,27,64</sup> were higher and in the range of 8.8-4.5 kJ mol<sup>-1</sup> at 0.02 <  $\theta$  < 0.8, in good agreement with the higher values found for  $\alpha$  when studying ACs.

Using only CACs, we found that  $\beta$ , the so-called entropy factor, was proportional to  $V_{T NLDFT}$ . We attributed this finding to a higher degree of disorder of the hydrogen molecules in wider pores <sup>6</sup>, because higher activation degrees are accompanied by pore widening as well as an increase in  $V_{T NLDFT}$ . **Figure 6d** shows that by plotting all  $\beta$  values together,  $\beta$  increases linearly with  $\bar{d}_\mu$  ( $R^2 = 0.92$ ), which can be due to the higher degree of disorder of H<sub>2</sub> molecules in materials with wider pores, in good agreement with the lower hydrogen densities achieved upon increasing the pore diameter <sup>67</sup>. Still, a linear tendency of  $\beta$  with  $V_{T NLDFT}$  was observed, but  $R^2$  was considerably lower (**Table S10**).

For all four MOFs,  $m$  was found in the range of 1.65 to 2.25, in line with the range of values that other authors have reported for MOFs <sup>16,19</sup>. **Figure 6e** shows that  $m$  increases with  $\bar{d}_\mu$ . In our previous study on CACs <sup>6</sup>,  $m$  was not fitted but set to 2 as has been done by other authors when using the MDA equation <sup>10,18,21,22</sup>. When fitting  $m$  as a function of  $\bar{d}_\mu$  for MOFs only, for which  $m$  has been fitted as another parameter of the MDA model,  $R^2$  was 0.96 (**Table S10**). In a future study, we will also determine  $m$  for CACs to clarify if there is a relationship between textural parameters and  $m$  for CACs as well.

Regarding the pseudo-saturation pressure,  $P_0$ , values between 130 and 976 MPa were found for MOFs, which are of the same order of magnitude as those reported by other authors <sup>10,16,18,19,21,22</sup>. For instance,  $P_0$  was found to be 322 <sup>22</sup> and 1246 <sup>16</sup> MPa for MOF-5, whereas values of 79 (for powder) and 215 (for pellets) MPa were reported for MOF-177 <sup>19</sup>. Although these pressures seem high,  $P_0$  was originally defined as the saturation pressure in Dubinin's

model for subcritical conditions. In contrast, hydrogen adsorption is usually studied under supercritical conditions<sup>38,40,41</sup>, so the original definition of  $P_0$  loses its physical meaning<sup>6</sup>. Therefore, Do and Do<sup>68</sup> suggested a concept of quasi-saturated vapor pressure based on the assumption that supercritical fluids could form clusters when confined in narrow micropores, and these clusters could be large enough to exert  $P_0$  in the same way as a subcritical fluid. In **Figure 6f**, the increase in  $P_0$  of MOFs and CACs as a function of  $\bar{d}_\mu$  is observed.  $R^2$  is 0.96 if only the MOFs are considered for the regression of  $P_0$  versus  $\bar{d}_\mu$  (**Table S10**). Such linear relationship is in good agreement with other authors who considered that  $P_0$  is not only characteristic of the adsorbate but also depends on the adsorbate-adsorbent interactions<sup>18,22</sup>. This aspect deserves more attention and we continue to work on it. Fitting the  $n_{exc}$  adsorption data including the parameter  $m$  as another parameter of the MDA model (thus with  $n_{max}$ ,  $\alpha$ ,  $\beta$ ,  $P_0$  and  $V_a$ ) for CACs could improve the linear tendency between  $P_0$  and  $\bar{d}_\mu$ . In addition, it has also been proposed that  $P_0$  could be temperature-dependent<sup>19,21</sup>. These approaches will be addressed in further studies.

#### 4.5 Release capacity

In practice, the performance of cryogenic compression adsorption systems is manifested by H<sub>2</sub> charge-discharge cycles and, therefore, optimal performance is limited by its ability to store through adsorption and compression, and release as much hydrogen as possible under operating conditions<sup>8,15,45</sup>. This can be quantified by the release or usable capacity,  $\Delta n_{H_2}$ , which is the amount of hydrogen released between the storage tank pressure and the back pressure for a fuel cell under operating conditions<sup>8,15,45,48</sup>. It can be calculated using the total uptake, as it takes into account the compressed gas in the void volume of the adsorbent material<sup>8,9,15,19</sup>. To calculate the release capacity, most of the studies estimates the pack density as equal to the single-crystal density<sup>8,15,50</sup>. **Table S11** shows the release capacities of MOFs reported in recent studies<sup>8,9,15,60</sup>

calculated employing single-crystal density. As discussed previously, we consider that using the tapped density would lead to more realistic estimates, but in order to compare the data obtained with the literature, we used both approaches to perform our calculations.

**Figure S8** shows the total hydrogen isotherms of the four MOFs calculated by Eq. (10) using tapped density, whereas **Figure S9** and **Figure S10** show the total hydrogen isotherms calculated on the basis of single-crystal density considering a regular close-packing of spherical grains and neglecting the packing, respectively. Using the total isotherms (**Figure S8**, **Figure S9** and **Figure S10**), the deliverable capacity of MOFs,  $\Delta n_{H_2}$ , was calculated considering a discharge, or back pressure, of 0.5 MPa and a charge pressure of 10 MPa. The results of the two scenarios considered: (i) an isothermal charge-discharge process<sup>15</sup> ( $\Delta n_{H_2}^{isothermal}$ ) at 77K, and (ii) a change of temperature from a charge at 77 K to a discharge at 160 K<sup>8,9,15</sup> ( $\Delta n_{H_2}^{77 \rightarrow 160 K}$ ), are reported in **Table S11** and **Table S12**. Furthermore, we estimated the  $\Delta n_{H_2}^{isothermal}$  and  $\Delta n_{H_2}^{77 \rightarrow 160 K}$  of MOFs reported in recent studies<sup>8,9,15,60</sup> from the data of **Table S11** by considering a regular packing of spherical grains ( $\rho_{pack} = 0.74 \rho_{cry}$ ). These results are presented in **Table S12**.

**Figure 8a-b** shows the evolution of  $\Delta n_{H_2}$  as a function of  $A_{BET}$  in MOFs when calculations are performed using: (a) the single-crystal density, and (b) the tapped density or the single-crystal density considering a regular packing of spherical grains ( $\rho_{pack} = 0.74 \rho_{cry}$ ). For MOFs with  $A_{BET}$  in the range of 681-6245 m<sup>2</sup> g<sup>-1</sup>,  $\Delta n_{H_2}^{isothermal}$  determined using single-crystal density is in the range 1.15-10.1 wt.% and increases linearly with  $A_{BET}$  (**Figure 8a**). The hydrogen release can be significantly enhanced when a change of temperature is made<sup>69</sup>. As discharge temperatures increase to 160 K,  $\Delta n_{H_2}^{77 \rightarrow 160 K}$  is in the range of 2.6-14 wt.% for MOFs having  $A_{BET}$  in the range of 681-7310 m<sup>2</sup> g<sup>-1</sup> and  $\Delta n_{H_2}^{77 \rightarrow 160 K}$  also increases linearly with  $A_{BET}$ . The release capacities determined for our MOFs using single-crystal density are in good agreement with data reported

in the open literature under the same conditions. **Figure 8b** shows the obtained  $\Delta n_{H_2}^{isothermal}$  (top) and the  $\Delta n_{H_2}^{77 \rightarrow 160 K}$  (bottom) calculated using the tapped density or the regular packing of spherical grains ( $\rho_{pack} = 0.74 \rho_{cry}$ ) from the literature<sup>8,9,15,60</sup>, plotted as a function of  $A_{BET}$ . It is interesting to note that the values obtained for the literature data when a regular packing is considered are consistent with those we obtained when the tapped density was employed. Indeed, the values of  $\Delta n_{H_2}$  obtained when the void volume of an ideal packing of spherical grains is taken into account (**Figure 8b**) are higher than those found using the single-crystal density alone. This is independent of the material used and may still underestimate the void volume as shown in Table S1, where it can be seen that the measured tapped densities are lower than  $0.74 \rho_{cry}$ . Moreover, the values of  $\Delta n_{H_2}^{77 \rightarrow 160 K}$  were also higher than  $\Delta n_{H_2}^{isothermic}$ , as when the single-crystal density was used in the calculation (**Figure 8a**), and the two release capacities increased with  $A_{BET}$ .

For a system charging at 77 K and 10 MPa (**Figure 8c**), around 70 % of the total hydrogen can be released by isothermal discharge (**Table S11** and **Figure 8d**). This percentage can increase to 94 % of the total hydrogen storage capacity when the system is heated to 160 K during discharge (**Table S11** and **Figure 8d**), which is consistent with literature results using single-crystal density (**Figure 8a**).

The storage capacity by simple compression in a 1 m<sup>3</sup> tank at 298 K and 70 MPa is 39 kg and the corresponding  $\Delta n_{H_2}^{isothermal}$  (at 298 K) is 38.6 kg, that is, 99% of the total H<sub>2</sub> stored. If the charge pressure is reduced to 10 MPa but the temperature is set at 77 K, the storage capacity of a 1 m<sup>3</sup> tank is reduced to 31.3 kg and  $\Delta n_{H_2}^{77 \rightarrow 160 K}$  is 29.7 kg, or 95%. Using the tapped density and Eq. (10), we estimated the mass of compressed and adsorbed hydrogen at 77 K and 10 MPa for a 1 m<sup>3</sup> tank filled with each MOF (**Figure 8c**). The total hydrogen storage is between 30 and 42 kg,

which is in the same range of values as the data reported by Dailly et al.<sup>19</sup> for MOF-177. Of the total stored amount, at least 94 % is usable when the discharge conditions are set at 160 K and 0.5 MPa (according to  $\Delta n_{H_2}^{77 \rightarrow 160 K}$ ) (**Table S11** and **Figure 8d**). Generally, at 77 K and 10 MPa, a reduction of the gas compressed in the system is observed when MOFs are introduced (blue region in **Figure 8c**), due to the reduction in void volume. However, the reduction in the amount of hydrogen stored by compression is almost compensated by the hydrogen adsorbed on MIL-53Al (3% less). Due to the contribution of hydrogen adsorbed on HKUST-1, MOF-177 and MOF-5, the amount of hydrogen stored is much higher than the compressed hydrogen in the same empty tank volume, and thus the hydrogen stored was 38.1, 41.2 and 42.0 kg per m<sup>3</sup>, respectively. Nevertheless, the amount of hydrogen stored by compression (around 60%) is significantly higher than that stored by adsorption at 77 K and 10 MPa. In terms of usable H<sub>2</sub>, a 16-33 % increase in  $\Delta n_{H_2}^{77 \rightarrow 160 K}$  is obtained when MOF-177, MOF-5 and HKUST-1 are introduced into the tank (red bars in **Figure 8d**) due to adsorption on MOFs.

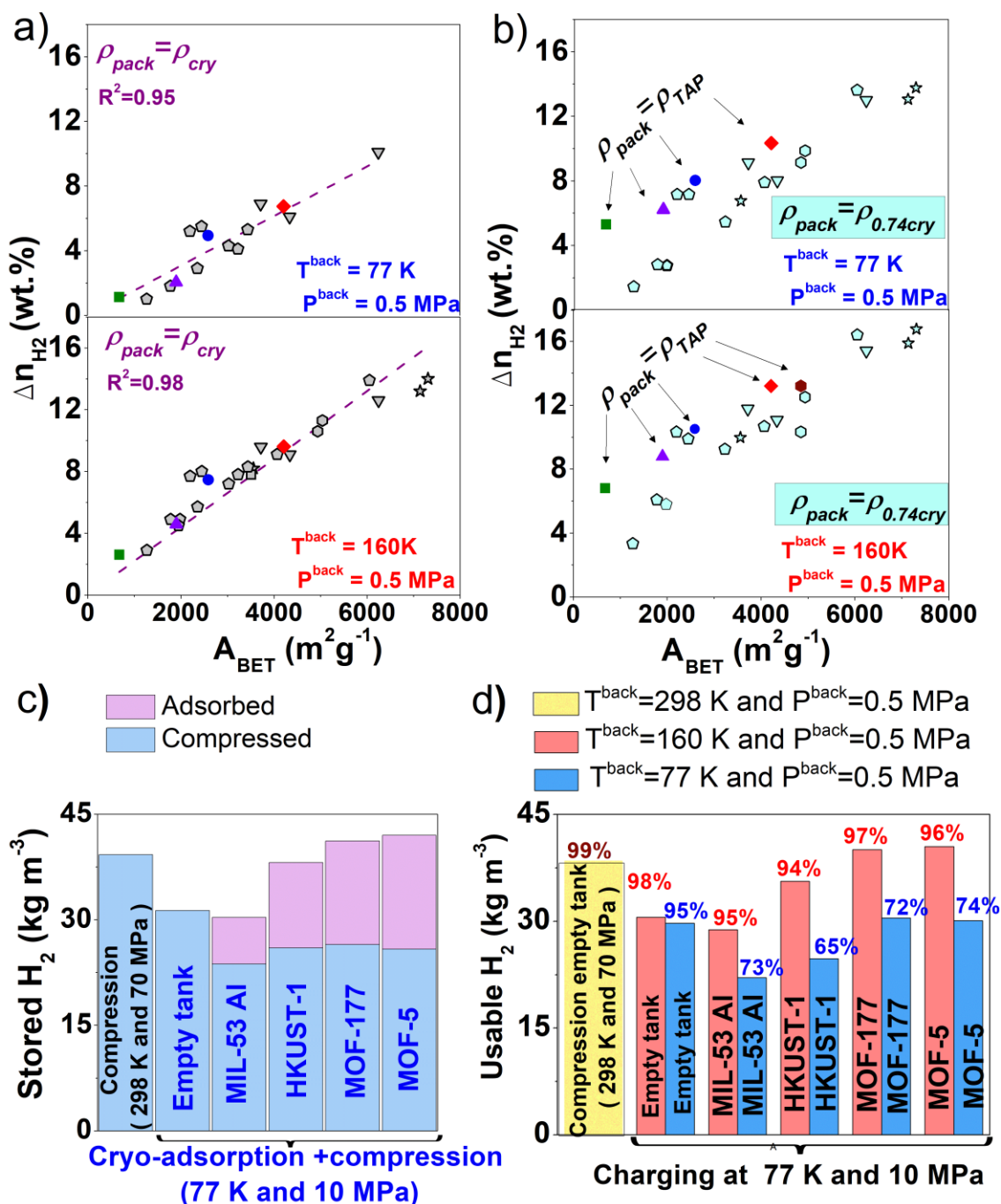


**Figure 8.** Evolution of hydrogen release capacity,  $\Delta n_{H_2}$ , as a function of  $A_{BET}$  in MOFs, determined using: (a) single-crystal density, and (b) tapped density or a regular packing of spherical grains ( $\rho_{pack} = 0.74 \rho_{cry}$ ). The data plotted are from recent studies ( $\diamond \square^{15}$ ,  $\star \star^8$ ,  $\nabla \nabla^9$ ,  $\square^{70}$ ,  $\diamond \square^{60}$ ) and this study ( $\blacksquare$  MIL-53AL,  $\bullet$  MOF-5,  $\blacktriangle$  HKUST-1,  $\blacklozenge$  MOF-177). The charge conditions considered are 77 K and 10 MPa while the discharge conditions are 77 K and 0.5 MPa, or 160 K and 0.5 MPa. Grey symbols ( $\diamond \star \nabla \square \circ$ ) corresponds to the literature reported release capacities calculated employing the single-crystal density. Empty symbols ( $\diamond \star \nabla \circ$ ) correspond to the release capacities of the

literature determinate when a regular steric packing is considered. Full colors symbols correspond to the release capacities determinate employing the TAP density (■●▲◆●). (c) H<sub>2</sub> storage for a tank filled with MOFs (MIL-53AL, MOF-5, HKUST-1, MOF-177) at 77 K and 10 MPa corresponding to adsorption (■), and compression (■). The data were calculated employing the tapped density. For comparison, H<sub>2</sub> storage of an empty tank is displayed at: (i) 298 K and 70 MPa, and (ii) 77 K and 10 MPa. d) Usable capacity of the systems shown in (c) when considering the following discharge temperatures and pressures: (■) 298 K and 0.5 MPa; (■) 160 K and 0.5 MPa; and (■) 77 K and 0.5 MPa. The percentage of usable H<sub>2</sub> from the total stored H<sub>2</sub> is shown above each column.

Compared to compression at 298 K and 70 MPa, cryogenic adsorption systems using MOF-177 and MOF-5 exhibited 5 and 7 % higher release capacity, respectively (**Figure 8d**). Therefore, the introduction of a porous solid of high surface area could lead to systems operating at lower pressures, which would therefore require less resistant materials than those used for room-temperature compression and would thus be more cost-effective.

**Figure 9a-b** displays the gravimetric profiles of  $\Delta n_{H_2}^{Ti \rightarrow 160 K}$  as a function of the charging temperature and pressure when the discharge conditions are 160 K and 0.5 MPa for MOF-5 and MOF-177. The corresponding volumetric profiles are shown in **Figure S11a-b**.

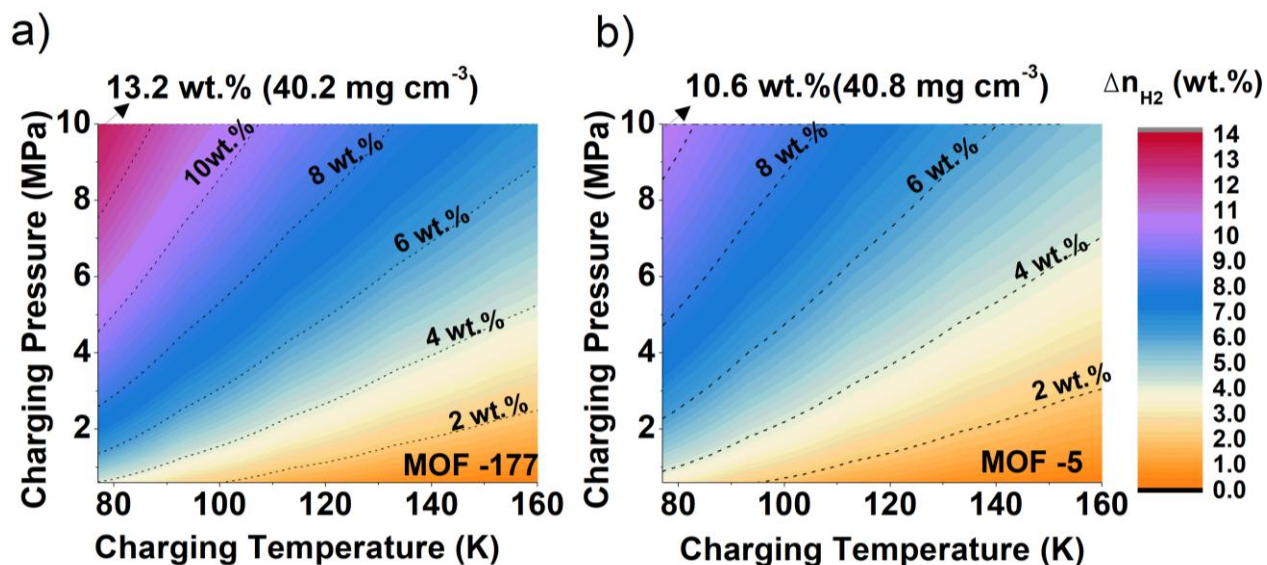




**Figure 9.** Gravimetric release capacity profile a function of the charging temperature and pressure, with discharge pressure and temperature equal to 0.5 MPa and 160 K, respectively for: (a) MOF-177; and (b) MOF-5.

In general, higher  $\Delta n_{H_2}^{T_i \rightarrow 160\text{ K}}$  are obtained at lower charging temperatures and higher charging pressures due to increased densities of the adsorbed and compressed phases<sup>10,37</sup>. Although MOF-177 has the highest H<sub>2</sub> release capacity on a gravimetric basis, 13.2 wt.%, and the second highest is MOF-5, 10.6 wt.% (see **Table S11** and **Figure 9a-b**), MOF-5 has the highest release capacity when the data are compared on a volumetric basis. MOF-5 can deliver 40.8 mg cm<sup>-3</sup> (**Figure S11b**) compared to the 40.2 mg cm<sup>-3</sup> that is released by MOF-177 (**Figure S11a**). This is related to the fact that the H<sub>2</sub> uptake in volumetric units tends to a constant value at high gravimetric H<sub>2</sub> uptake for materials of high  $A_{BET}$ <sup>13</sup> (see Section 4.2). Therefore, among the four MOFs studied, the material with the highest usable hydrogen storage is MOF-5.

## 5. Conclusions

In this study, we have successfully fitted the experimental excess hydrogen adsorption on four commercial nanoporous Metal-Organic Frameworks (MOFs): MIL53-Al, MOF-5, HKUST-1 and MOF-177 over a wide range of pressures and temperatures using the Modified Dubinin-Astakhov (MDA) equation. The parameters  $n_{max}$ ,  $V_a$ ,  $\alpha$ ,  $\beta$ ,  $m$  and  $P_0$  were correlated to the textural properties of the MOFs.  $n_{max}$  and  $V_a$  are directly proportional to the BET area. The “entropy” factor,  $\beta$ , linearly increases with the average micropore diameter whereas the “enthalpy” factor,  $\alpha$ , is inversely proportional to the average micropore diameter and directly proportional to the ultramicropore volume. Moreover, we observed that the factors  $P_0$  and  $m$  increase with the average micropore size. From the enthalpy” factor  $\alpha$ , we determined the isosteric heat of

adsorption. At near-zero surface coverage, for  $\theta = 0.05$ , values between 3.7 and 6.7 kJ mol<sup>-1</sup> were obtained for the four MOFs, which are consistent with those reported in the literature.

Total hydrogen isotherms were calculated based on the single-crystal density of the MOFs although it neglects the void volume between grains, since MOFs are powdery materials in practice. Therefore, it does not take into account the contribution of compressed gas in systems at pressures above 5 MPa, which induces serious errors. We proposed to consider an ideal, regular close-packing of spherical grains, which has a compactness of 74%, when the data of tapped density is not available.

Using total adsorption isotherms, we determined their hydrogen release capacities from a charging pressure of 10 MPa to a discharge pressure of 0.5 MPa. The release capacities are enhanced when increasing the discharge temperature up to 160K. Under these charge-discharge conditions, the introduction of a MOF of high surface area significantly improves the hydrogen release capacity compared to an empty tank. Furthermore, the comparison between release capacities expressed on volumetric and gravimetric bases proves that the materials offering the highest gravimetric storage capacities are not necessarily those offering the highest volumetric capacities.

## Acknowledgements

Pamela Ramirez-Vidal gratefully acknowledges the financial support of CONACYT-SENER (scholarship: 708651/739301). This study was partly supported by ANR-15-IDEX-04-LUE and TALiSMAN project (2019-000214, funded by ERDF). The authors thank Philippe Gadonneix for his technical assistance in the laboratory measurements.

## Supporting Information

Results of the textural characterisation of the samples; H<sub>2</sub> and CO<sub>2</sub> uptakes up to 0.1 MPa; Henry's law constants of MOFs for H<sub>2</sub> and CO<sub>2</sub> adsorption; excess H<sub>2</sub> uptake at 77 K and 2-3 MPa and at 273 and 14 MPa; results obtained from the linear regression of the excess H<sub>2</sub> plotted against the density of the gas phase in the saturation regime; textural properties and H<sub>2</sub> uptakes of different MOFs reported in the literature; total hydrogen adsorption isotherms of the samples; MDA parameters of the samples and the determination coefficient obtained when linearly fitting them to their textural properties; H<sub>2</sub> release capacity of different MOFs reported in the literature.

## References

- (1) Sdanghi, G.; Maranzana, G.; Celzard, A.; Fierro, V. Towards Non-Mechanical Hybrid Hydrogen Compression for Decentralized Hydrogen Facilities. *Energies* **2020**, *13* (12), 3145. <https://doi.org/10.3390/en13123145>.
- (2) Aceves, S. M.; Petitpas, G.; Espinosa-Loza, F.; Matthews, M. J.; Ledesma-Orozco, E. Safe, Long Range, Inexpensive and Rapidly Refuelable Hydrogen Vehicles with Cryogenic Pressure Vessels. *International Journal of Hydrogen Energy* **2013**, *38* (5), 2480–2489. <https://doi.org/10.1016/j.ijhydene.2012.11.123>.
- (3) Andersson, J.; Grönkvist, S. Large-Scale Storage of Hydrogen. *International Journal of Hydrogen Energy* **2019**, *44* (23), 11901–11919. <https://doi.org/10.1016/j.ijhydene.2019.03.063>.
- (4) Meneghelli, B.; Tamburello, D.; Fesmire, J.; Swanger, A. IV.D.4 Integrated Insulation System for Automotive Cryogenic Storage Tanks. **2017**, 6.
- (5) Bellosta von Colbe, J.; Ares, J.-R.; Barale, J.; Baricco, M.; Buckley, C.; Capurso, G.; Gallandat, N.; Grant, D. M.; Guzik, M. N.; Jacob, I.; Jensen, E. H.; Jensen, T.; Jepsen, J.; Klassen, T.; Lototsky, M. V.; Manickam, K.; Montone, A.; Puszkiel, J.; Sartori, S.;

- Sheppard, D. A.; Stuart, A.; Walker, G.; Webb, C. J.; Yang, H.; Yartys, V.; Züttel, A.; Dornheim, M. Application of Hydrides in Hydrogen Storage and Compression: Achievements, Outlook and Perspectives. *International Journal of Hydrogen Energy* **2019**, *44* (15), 7780–7808. <https://doi.org/10.1016/j.ijhydene.2019.01.104>.
- (6) Ramirez-Vidal, P.; Canevesi, R. L. S.; Sdanghi, G.; Schaefer, S.; Maranzana, G.; Celzard, A.; Fierro, V. A Step Forward in Understanding the Hydrogen Adsorption and Compression on Activated Carbons. *ACS Appl. Mater. Interfaces* **2021**, *13* (10), 12562–12574. <https://doi.org/10.1021/acsami.0c22192>.
- (7) Cousins, K.; Zhang, R. Highly Porous Organic Polymers for Hydrogen Fuel Storage. *Polymers* **2019**, *11* (4), 690. <https://doi.org/10.3390/polym11040690>.
- (8) Chen, Z.; Li, P.; Anderson, R.; Wang, X.; Zhang, X.; Robison, L.; Redfern, L. R.; Moribe, S.; Islamoglu, T.; Gómez-Gualdrón, D. A.; Yildirim, T.; Stoddart, J. F.; Farha, O. K. Balancing Volumetric and Gravimetric Uptake in Highly Porous Materials for Clean Energy. *Science* **2020**, *368* (6488), 8. <https://doi.org/10.1126/science.aaz8881>.
- (9) Gómez-Gualdrón, D. A.; Wang, T. C.; García-Holley, P.; Sawelewa, R. M.; Argueta, E.; Snurr, R. Q.; Hupp, J. T.; Yildirim, T.; Farha, O. K. Understanding Volumetric and Gravimetric Hydrogen Adsorption Trade-off in Metal–Organic Frameworks. *ACS Appl. Mater. Interfaces* **2017**, *9* (39), 33419–33428. <https://doi.org/10.1021/acsami.7b01190>.
- (10) Sdanghi, G.; Schaefer, S.; Maranzana, G.; Celzard, A.; Fierro, V. Application of the Modified Dubinin-Astakhov Equation for a Better Understanding of High-Pressure Hydrogen Adsorption on Activated Carbons. *International Journal of Hydrogen Energy* **2020**, *45* (48), 25912–25926. <https://doi.org/10.1016/j.ijhydene.2019.09.240>.
- (11) Ahluwalia, R. K.; Hua, T. Q.; Peng, J.-K.; Lasher, S.; McKenney, K.; Sinha, J.; Gardiner, M. Technical Assessment of Cryo-Compressed Hydrogen Storage Tank Systems for Automotive Applications. *International Journal of Hydrogen Energy* **2010**, *35* (9), 4171–4184. <https://doi.org/10.1016/j.ijhydene.2010.02.074>.
- (12) Siegel, D.; Hardy, B. Engineering an Adsorbent-Based Hydrogen Storage System: What Have We Learned?; HSECoE Team., 2021.
- (13) Balderas- Xicohténcatl, R.; Schlichtenmayer, M.; Hirscher, M. Volumetric Hydrogen Storage Capacity in Metal–Organic Frameworks. *Energy Technology* **2018**, *6* (3), 578–582. <https://doi.org/10.1002/ente.201700636>.
- (14) Fairen-Jimenez, D.; Colón, Y. J.; Farha, O. K.; Bae, Y.-S.; Hupp, J. T.; Snurr, R. Q. Understanding Excess Uptake Maxima for Hydrogen Adsorption Isotherms in Frameworks with Rht Topology. *Chem. Commun.* **2012**, *48* (85), 10496. <https://doi.org/10.1039/c2cc35711a>.
- (15) García-Holley, P.; Schweitzer, B.; Islamoglu, T.; Liu, Y.; Lin, L.; Rodriguez, S.; Weston, M. H.; Hupp, J. T.; Gómez-Gualdrón, D. A.; Yildirim, T.; Farha, O. K. Benchmark Study of Hydrogen Storage in Metal–Organic Frameworks under Temperature and Pressure Swing Conditions. *ACS Energy Lett.* **2018**, *3* (3), 748–754. <https://doi.org/10.1021/acsenergylett.8b00154>.
- (16) Sridhar, P.; Kaisare, N. S. A Critical Analysis of Transport Models for Refueling of MOF-5 Based Hydrogen Adsorption System. *Journal of Industrial and Engineering Chemistry* **2020**, *85*, 170–180. <https://doi.org/10.1016/j.jiec.2020.01.038>.
- (17) Zhang, X.; Zheng, Q.; Zhao, G.; Zhang, W. Adsorption Equilibrium and Charge/Discharge Characteristics of Hydrogen on MOFs. *Cryogenics* **2020**, *112*, 103121. <https://doi.org/10.1016/j.cryogenics.2020.103121>.

- (18) Richard, M.-A.; Bénard, P.; Chahine, R. Gas Adsorption Process in Activated Carbon over a Wide Temperature Range above the Critical Point. Part 1: Modified Dubinin-Astakhov Model. *Adsorption* **2009**, *15* (1), 43–51. <https://doi.org/10.1007/s10450-009-9149-x>.
- (19) Dailly, A.; Poirier, E. Evaluation of an Industrial Pilot Scale Densified MOF-177 Adsorbent as an on-Board Hydrogen Storage Medium. *Energy Environ. Sci.* **2011**, *4* (9), 3527. <https://doi.org/10.1039/c1ee01426a>.
- (20) Poirier, E.; Dailly, A. Investigation of the Hydrogen State in IRMOF-1 from Measurements and Modeling of Adsorption Isotherms at High Gas Densities. *J. Phys. Chem. C* **2008**, *112* (33), 13047–13052. <https://doi.org/10.1021/jp800981f>.
- (21) Richard, M.-A.; Bénard, P.; Chahine, R. Gas Adsorption Process in Activated Carbon over a Wide Temperature Range above the Critical Point. Part 2: Conservation of Mass and Energy. *Adsorption* **2009**, *15* (1), 53–63. <https://doi.org/10.1007/s10450-009-9150-4>.
- (22) Hardy, B.; Corgnale, C.; Chahine, R.; Richard, M.-A.; Garrison, S.; Tamburello, D.; Cossement, D.; Anton, D. Modeling of Adsorbent Based Hydrogen Storage Systems. *International Journal of Hydrogen Energy* **2012**, *37* (7), 5691–5705. <https://doi.org/10.1016/j.ijhydene.2011.12.125>.
- (23) Kim, S.-Y.; Kang, J. H.; Kim, S.-I.; Bae, Y.-S. Extraordinarily Large and Stable Methane Delivery of MIL-53(Al) under LNG-ANG Conditions. *Chemical Engineering Journal* **2019**, *365*, 242–248. <https://doi.org/10.1016/j.cej.2019.01.182>.
- (24) Li, H.; Eddaoudi, M.; O’Keeffe, M.; Yaghi, O. M. Design and Synthesis of an Exceptionally Stable and Highly Porous Metal-Organic Framework. **1999**, *402*, 4.
- (25) Furukawa, H.; Ko, N.; Go, Y. B.; Aratani, N.; Choi, S. B.; Choi, E.; Yazaydin, A. O.; Snurr, R. Q.; O’Keeffe, M.; Kim, J.; Yaghi, O. M. Ultrahigh Porosity in Metal-Organic Frameworks. *Science* **2010**, *329* (5990), 424–428. <https://doi.org/10.1126/science.1192160>.
- (26) Furukawa, H.; Miller, M. A.; Yaghi, O. M. Independent Verification of the Saturation Hydrogen Uptake in MOF-177 and Establishment of a Benchmark for Hydrogen Adsorption in Metal–Organic Frameworks. *J. Mater. Chem.* **2007**, *17* (30), 3197. <https://doi.org/10.1039/b703608f>.
- (27) Schlichtenmayer, M.; Hirscher, M. Nanosponges for Hydrogen Storage. *J. Mater. Chem.* **2012**, *22* (20), 10134. <https://doi.org/10.1039/c2jm15890f>.
- (28) Boutin, A.; Coudert, F.-X.; Springuel-Huet, M.-A.; Neimark, A. V.; Férey, G.; Fuchs, A. H. The Behavior of Flexible MIL-53(Al) upon CH<sub>4</sub> and CO<sub>2</sub> Adsorption. *J. Phys. Chem. C* **2010**, *114* (50), 22237–22244. <https://doi.org/10.1021/jp108710h>.
- (29) Rowsell, J. L. C.; Yaghi, O. M. Strategies for Hydrogen Storage in Metal–Organic Frameworks. *Angewandte Chemie International Edition* **2005**, *44* (30), 4670–4679. <https://doi.org/10.1002/anie.200462786>.
- (30) Schoedel, A.; Yaghi, O. M. Porosity in Metal-Organic Compounds. In *Macrocyclic and Supramolecular Chemistry*; Izatt, R. M., Ed.; John Wiley & Sons, Ltd: Chichester, UK, 2016; pp 200–219. <https://doi.org/10.1002/9781119053859.ch9>.
- (31) Moran, C. M.; Joshi, J. N.; Marti, R. M.; Hayes, S. E.; Walton, K. S. Structured Growth of Metal–Organic Framework MIL-53(Al) from Solid Aluminum Carbide Precursor. *J. Am. Chem. Soc.* **2018**, *140* (29), 9148–9153. <https://doi.org/10.1021/jacs.8b04369>.
- (32) Rouquerol, J.; Llewellyn, P.; Rouquerol, F. Is the Bet Equation Applicable to Microporous Adsorbents? In *Studies in Surface Science and Catalysis*; Llewellyn, P. L., Rodriguez-Reinoso, F., Rouquerol, J., Seaton, N., Eds.; Characterization of Porous Solids VII; Elsevier, 2007; Vol. 160, pp 49–56. [https://doi.org/10.1016/S0167-2991\(07\)80008-5](https://doi.org/10.1016/S0167-2991(07)80008-5).

- (33) Rabbani, M. G.; Sekizkardes, A. K.; Kahveci, Z.; Reich, T. E.; Ding, R.; El-Kaderi, H. M. A 2D Mesoporous Imine-Linked Covalent Organic Framework for High Pressure Gas Storage Applications. *Chemistry – A European Journal* **2013**, *19* (10), 3324–3328. <https://doi.org/10.1002/chem.201203753>.
- (34) Jagiello, J.; Kenvin, J.; Ania, C. O.; Parra, J. B.; Celzard, A.; Fierro, V. Exploiting the Adsorption of Simple Gases O<sub>2</sub> and H<sub>2</sub> with Minimal Quadrupole Moments for the Dual Gas Characterization of Nanoporous Carbons Using 2D-NLDFT Models. *Carbon* **2020**, *160*, 164–175. <https://doi.org/10.1016/j.carbon.2020.01.013>.
- (35) Dubinin, M. M. Adsorption in Micropores. *Journal of Colloid and Interface Science* **1967**, *23* (4), 487–499. [https://doi.org/10.1016/0021-9797\(67\)90195-6](https://doi.org/10.1016/0021-9797(67)90195-6).
- (36) Kadono, K.; Kajiura, H.; Shiraishi, M. Dense Hydrogen Adsorption on Carbon Subnanopores at 77 K. *Appl. Phys. Lett.* **2003**, *83* (16), 3392–3394. <https://doi.org/10.1063/1.1621073>.
- (37) Poirier, E.; Dailly, A. On the Nature of the Adsorbed Hydrogen Phase in Microporous Metal–Organic Frameworks at Supercritical Temperatures. *Langmuir* **2009**, *25* (20), 12169–12176. <https://doi.org/10.1021/la901680p>.
- (38) Jagiello, J.; Ansón, A.; Martínez, M. T. DFT-Based Prediction of High-Pressure H<sub>2</sub> Adsorption on Porous Carbons at Ambient Temperatures from Low-Pressure Adsorption Data Measured at 77 K. *J. Phys. Chem. B* **2006**, *110* (10), 4531–4534. <https://doi.org/10.1021/jp057340x>.
- (39) Silvera, I. F. The Solid Molecular Hydrogens in the Condensed Phase: Fundamentals and Static Properties. *Rev. Mod. Phys.* **1980**, *52* (2), 393–452. <https://doi.org/10.1103/RevModPhys.52.393>.
- (40) Romanos, J.; Abou Dargham, S.; Roukos, R.; Pfeifer, P. Local Pressure of Supercritical Adsorbed Hydrogen in Nanopores. *Materials* **2018**, *11* (11), 2235. <https://doi.org/10.3390/ma11112235>.
- (41) Sharpe, J. E.; Bimbo, N.; Ting, V. P.; Burrows, A. D.; Jiang, D.; Mays, T. J. Supercritical Hydrogen Adsorption in Nanostructured Solids with Hydrogen Density Variation in Pores. *Adsorption* **2013**, *19* (2), 643–652. <https://doi.org/10.1007/s10450-013-9487-6>.
- (42) Hurst, K. E.; Gennett, T.; Adams, J.; Allendorf, M. D.; Balderas-Xicohténcatl, R.; Bielewski, M.; Edwards, B.; Espinal, L.; Fultz, B.; Hirscher, M.; Hudson, M. S. L.; Hulvey, Z.; Latroche, M.; Liu, D.-J.; Kapelewski, M.; Napolitano, E.; Perry, Z. T.; Purewal, J.; Stavila, V.; Veenstra, M.; White, J. L.; Yuan, Y.; Zhou, H.-C.; Zlotea, C.; Parilla, P. An International Laboratory Comparison Study of Volumetric and Gravimetric Hydrogen Adsorption Measurements. *ChemPhysChem* **2019**, *20* (15), 1997–2009. <https://doi.org/10.1002/cphc.201900166>.
- (43) Poirier, E.; Dailly, A. Thermodynamic Study of the Adsorbed Hydrogen Phase in Cu-Based Metal-Organic Frameworks at Cryogenic Temperatures. *Energy Environ. Sci.* **2009**, *2* (4), 420. <https://doi.org/10.1039/b818393g>.
- (44) Levenberg, K. A Method for the Solution of Certain Non-Linear Problems in Least Squares. *Quarterly of Applied Mathematics* **1944**, *2* (2), 164–168.
- (45) Schlichtenmayer, M.; Hirscher, M. The Usable Capacity of Porous Materials for Hydrogen Storage. *Appl. Phys. A* **2016**, *122* (4), 379. <https://doi.org/10.1007/s00339-016-9864-6>.
- (46) Gedrich, K.; Senkowska, I.; Klein, N.; Stoeck, U.; Henschel, A.; Lohe, M. R.; Baburin, I. A.; Mueller, U.; Kaskel, S. A Highly Porous Metal–Organic Framework with Open Nickel Sites. *Angewandte Chemie International Edition* **2010**, *49* (45), 8489–8492. <https://doi.org/10.1002/anie.201001735>.

- (47) Zhu, H. H.; Fuh, J. Y. H.; Lu, L. The Influence of Powder Apparent Density on the Density in Direct Laser-Sintered Metallic Parts. *International Journal of Machine Tools and Manufacture* **2007**, *47* (2), 294–298. <https://doi.org/10.1016/j.ijmachtools.2006.03.019>.
- (48) Bastos-Neto, M.; Patzschke, C.; Lange, M.; Möllmer, J.; Möller, A.; Fichtner, S.; Schrage, C.; Lässig, D.; Lincke, J.; Staudt, R.; Krautscheid, H.; Gläser, R. Assessment of Hydrogen Storage by Physisorption in Porous Materials. *Energy Environ. Sci.* **2012**, *5* (8), 8294–8303. <https://doi.org/10.1039/C2EE22037G>.
- (49) Thommes, M.; Kaneko, K.; Neimark, A. V.; Olivier, J. P.; Rodriguez-Reinoso, F.; Rouquerol, J.; Sing, K. S. W. Physisorption of Gases, with Special Reference to the Evaluation of Surface Area and Pore Size Distribution (IUPAC Technical Report). *Pure and Applied Chemistry* **2015**, *87* (9–10), 1051–1069. <https://doi.org/10.1515/pac-2014-1117>.
- (50) Gómez-Gualdrón, D. A.; Moghadam, P. Z.; Hupp, J. T.; Farha, O. K.; Snurr, R. Q. Application of Consistency Criteria To Calculate BET Areas of Micro- And Mesoporous Metal–Organic Frameworks. *J. Am. Chem. Soc.* **2016**, *138* (1), 215–224. <https://doi.org/10.1021/jacs.5b10266>.
- (51) Zhang, X.; Lin, R.; Wang, J.; Wang, B.; Liang, B.; Yildirim, T.; Zhang, J.; Zhou, W.; Chen, B. Optimization of the Pore Structures of MOFs for Record High Hydrogen Volumetric Working Capacity. *Adv. Mater.* **2020**, *32* (17), 1907995. <https://doi.org/10.1002/adma.201907995>.
- (52) Sdanghi, G.; Maranzana, G.; Celzard, A.; Fierro, V. Hydrogen Adsorption on Nanotextured Carbon Materials. In *Hydrogen Storage Technologies*; John Wiley & Sons, Ltd, 2018; pp 263–320. <https://doi.org/10.1002/9781119460572.ch9>.
- (53) Fierro, V.; Szczurek, A.; Zlotea, C.; Marêché, J. F.; Izquierdo, M. T.; Albinia, A.; Latroche, M.; Furdin, G.; Celzard, A. Experimental Evidence of an Upper Limit for Hydrogen Storage at 77K on Activated Carbons. *Carbon* **2010**, *48* (7), 1902–1911. <https://doi.org/10.1016/j.carbon.2010.01.052>.
- (54) Furukawa, H.; Cordova, K. E.; O’Keeffe, M.; Yaghi, O. M. The Chemistry and Applications of Metal-Organic Frameworks. *Science* **2013**, *341* (6149), 1230444. <https://doi.org/10.1126/science.1230444>.
- (55) Rosi, N. L.; Eckert, J.; Eddaoudi, M.; Vodak, D. T.; Kim, J.; O’Keeffe, M.; Yaghi, O. M. Hydrogen Storage in Microporous Metal-Organic Frameworks. *Science* **2003**, *300* (5622), 1127–1129. <https://doi.org/10.1126/science.1083440>.
- (56) Farha, O. K.; Eryazici, I.; Jeong, N. C.; Hauser, B. G.; Wilmer, C. E.; Sarjeant, A. A.; Snurr, R. Q.; Nguyen, S. T.; Yazaydin, A. Ö.; Hupp, J. T. Metal–Organic Framework Materials with Ultrahigh Surface Areas: Is the Sky the Limit? *J. Am. Chem. Soc.* **2012**, *134* (36), 15016–15021. <https://doi.org/10.1021/ja3055639>.
- (57) Rouquerol, F.; Rouquerol, J.; Sing, K. S. W. 2 - Thermodynamics of Adsorption at the Gas/Solid Interface. In *Adsorption by Powders and Porous Solids (Second Edition)*; Rouquerol, F., Rouquerol, J., Sing, K. S. W., Llewellyn, P., Maurin, G., Eds.; Academic Press: Oxford, 2014; pp 25–56. <https://doi.org/10.1016/B978-0-08-097035-6.00002-4>.
- (58) Yurduşen, A.; Yürüm, A.; Yürüm, Y. A Remarkable Increase in the Adsorbed H<sub>2</sub> Amount: Influence of Pore Size Distribution on the H<sub>2</sub> Adsorption Capacity of Fe-BTC. *International Journal of Hydrogen Energy* **2020**, S0360319920308466. <https://doi.org/10.1016/j.ijhydene.2020.02.202>.

- (59) Sing, K. S. W. 5 - Classical Interpretation of Physisorption Isotherms at the Gas-Solid Interface. In *Adsorption by Powders and Porous Solids*; p 31.
- (60) Ahmed, A.; Seth, S.; Purewal, J.; Wong-Foy, A. G.; Veenstra, M.; Matzger, A. J.; Siegel, D. J. Exceptional Hydrogen Storage Achieved by Screening Nearly Half a Million Metal-Organic Frameworks. *Nat Commun* **2019**, *10* (1), 1568. <https://doi.org/10.1038/s41467-019-09365-w>.
- (61) Denysenko, D.; Grzywa, M.; Tonigold, M.; Streppel, B.; Krkljus, I.; Hirscher, M.; Mugnaioli, E.; Kolb, U.; Hanss, J.; Volkmer, D. Elucidating Gating Effects for Hydrogen Sorption in MFU-4-Type Triazolate-Based Metal-Organic Frameworks Featuring Different Pore Sizes. *Chem. Eur. J.* **2011**, *17* (6), 1837–1848. <https://doi.org/10.1002/chem.201001872>.
- (62) Brunauer, S.; Emmett, P. H.; Teller, E. Adsorption of Gases in Multimolecular Layers. *J. Am. Chem. Soc.* **1938**, *60* (2), 309–319. <https://doi.org/10.1021/ja01269a023>.
- (63) Wang, T. C.; Bury, W.; Gómez-Gualdrón, D. A.; Vermeulen, N. A.; Mondloch, J. E.; Deria, P.; Zhang, K.; Moghadam, P. Z.; Sarjeant, A. A.; Snurr, R. Q.; Stoddart, J. F.; Hupp, J. T.; Farha, O. K. Ultrahigh Surface Area Zirconium MOFs and Insights into the Applicability of the BET Theory. *J. Am. Chem. Soc.* **2015**, *137* (10), 3585–3591. <https://doi.org/10.1021/ja512973b>.
- (64) Schlichtenmayer, M.; Streppel, B.; Hirscher, M. Hydrogen Physisorption in High SSA Microporous Materials – A Comparison between AX-21\_33 and MOF-177 at Cryogenic Conditions. *International Journal of Hydrogen Energy* **2011**, *36* (1), 586–591. <https://doi.org/10.1016/j.ijhydene.2010.09.057>.
- (65) Wang, H.; Gao, Q.; Hu, J. High Hydrogen Storage Capacity of Porous Carbons Prepared by Using Activated Carbon. *J. Am. Chem. Soc.* **2009**, *131* (20), 7016–7022. <https://doi.org/10.1021/ja8083225>.
- (66) Bénard, P.; Chahine, R. Storage of Hydrogen by Physisorption on Carbon and Nanostructured Materials. *Scripta Materialia* **2007**, *56* (10), 803–808. <https://doi.org/10.1016/j.scriptamat.2007.01.008>.
- (67) Sdanghi, G.; Canevesi, R. L. S.; Celzard, A.; Thommes, M.; Fierro, V. Characterization of Carbon Materials for Hydrogen Storage and Compression. *C* **2020**, *6* (3), 46. <https://doi.org/10.3390/c6030046>.
- (68) Do, D. D.; Do, H. D. Adsorption of Supercritical Fluids in Non-Porous and Porous Carbons: Analysis of Adsorbed Phase Volume and Density. *Carbon* **2003**, *41* (9), 1777–1791. [https://doi.org/10.1016/S0008-6223\(03\)00152-0](https://doi.org/10.1016/S0008-6223(03)00152-0).
- (69) Ahluwalia, R. K.; Peng, J. K. Automotive Hydrogen Storage System Using Cryo-Adsorption on Activated Carbon. *International Journal of Hydrogen Energy* **2009**, *34* (13), 5476–5487. <https://doi.org/10.1016/j.ijhydene.2009.05.023>.
- (70) Ahmed, A.; Liu, Y.; Purewal, J.; Tran, L. D.; Wong-Foy, A. G.; Veenstra, M.; Matzger, A. J.; Siegel, D. J. Balancing Gravimetric and Volumetric Hydrogen Density in MOFs. *Energy Environ. Sci.* **2017**, *10* (11), 2459–2471. <https://doi.org/10.1039/C7EE02477K>.